



Seasonal and interannual (ENSO) climate variabilities and trends in the South China Sea over the last three decades

Violaine Piton ^(1,2) and Thierry Delcroix ⁽¹⁾

⁽¹⁾ LEGOS, CNES, CNRS, IRD, UPS, University of Toulouse, France

⁽²⁾ University of Sciences and Technology of Hanoi, Hanoi, Vietnam

Corresponding author: thierry.delcroix@legos.obs-mip.fr



1 **Abstract**

2 We present a short overview of the long-term mean and variability of five Essential Climate
3 Variables observed in the South China Sea over the last 3 decades, including sea surface
4 temperature (SST), sea level anomaly (SLA), precipitation (P), surface wind and water
5 discharge (WD) from the Mekong and Red Rivers. At the seasonal time scale, SST and SLAs
6 increase in the summer (up to 4.2°C and 14 cm, respectively), and P increases in the north.
7 The summer zonal and meridional winds reverse and intensify (mostly over the ocean), and
8 the WD shows positive anomalies. At the interannual time scale, each variable appears to be
9 correlated with El Niño Southern Oscillation (ENSO) indices. Eastern Pacific El Niño events
10 produce basin-wide SST warming (up to 1.4°C) with a 6-month lag. The SLAs fall basin-wide
11 (by up to 9 cm) during an El Niño event, with a 3-month lag. The zonal and meridional winds
12 strengthen (up to 4 m/s) in the north (weaken in the south) during all types of El Niño
13 events, with a 3-5-month lag. A rainfall deficit of approximately 30% of the mean occurs
14 during all types of El Niño phases. The Mekong River WD is reduced by 1/3 of the mean 7-8
15 months after all types of El Niño events. We also show increasing trends of SST as high as
16 0.24°C/decade and SLAs by 41 mm/decade. Increasing trends are observed for zonal wind,
17 which is possibly linked to the phase of the Pacific Decadal Oscillation, and decreasing trends
18 are observed for P in the north and both WD stations that were analyzed. The likely driving
19 mechanisms and some of the relationships between all observed anomalies are discussed.

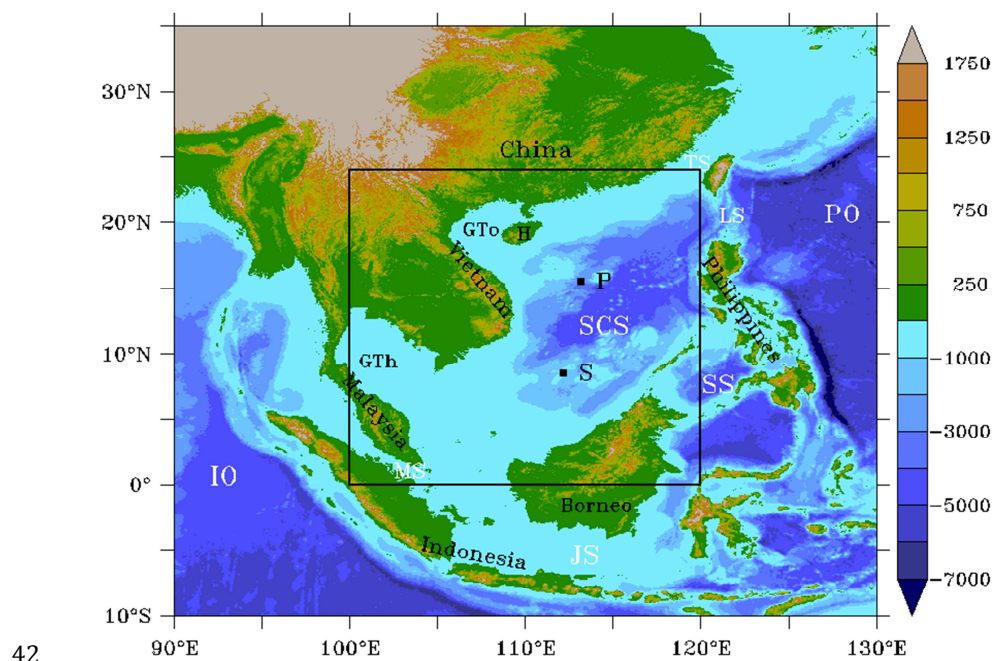
20
21
22
23
24
25
26
27
28
29
30
31

Keywords: ENSO, trends, climate variability, essential climate variable, South China Sea, seasonal variability



32 **1. Introduction**

33 The South China Seas (hereafter, SCS) is the largest marginal sea in Southeast Asia
34 and covers an area of 3.8 million km² from approximately 0-23°N and 99°E-121°E (Fig. 1).
35 This semi-closed basin is surrounded by South China, the Indochina Peninsula, Borneo and
36 the Philippines. It is open to the East China Sea through the Taiwan Strait, to the Pacific
37 through the Luzon Strait and to the Indian Ocean through the Malacca Strait and other
38 narrow straits. The SCS is the second busiest maritime route in the world; its topography is
39 rather complex with an average depth of 2000 m and maximum depths reaching 5000 m in
40 the northeast. There are wide and shallow continental shelves in the northwest and
41 southwest of the SCS and numerous islands such as Hainan, Paracel and Spratly.



42
43 **Figure 1.** Bathymetry below sea level and topography above sea level (in m) of the South
44 China Sea region. Our research domain is enclosed with a black rectangle. The acronyms
45 denote, *GTh* Gulf of Thailand, *GTo* Gulf of Tonkin, *H* Hainan island, *IO* Indian Ocean, *JS* Java
46 Sea, *MS* Malacca Strait, *LS* Luzon Strait, *TS* Taiwan Strait, *P* Paracel Islands, *PO* Pacific Ocean,



47 S Spratly Islands, SCS South China Sea, and SS Sulu Sea. The bathymetry intervals are from 0
48 to 1000 m, and the topography intervals are from 0 to 250 m.

49 Located in the tropical Northern Hemisphere, the SCS region is influenced by both a
50 tropical and a subtropical climate, by the four adjacent monsoon subsystems, as well as by
51 the inflow from and the outflow to the surrounding oceans (see the reviews by Wang et al.,
52 2009, and Qu et al., 2009). At the annual time scale, the climate is mainly determined by two
53 alternative monsoon cycles, a southwest monsoon that brings wet and warm weather over
54 the area in the boreal summer (hereafter, all seasons will refer to the northern hemisphere
55 seasons) and a northeast monsoon that brings cold and dry conditions in the winter (Wyrтки,
56 1961; Wang and LinHo, 2002; Nguyen et al., 2014). Moreover, at the interannual time scale,
57 the SCS region is further influenced by the El Niño-Southern Oscillation (ENSO) phenomena.
58 Several studies have been conducted on the interannual (ENSO) variability of the SCS in
59 terms of sea surface temperature (Huynh et al., 2016; Liu et al., 2014; Tan et al., 2016; Yang
60 et al., 2015; Wang et al., 2006), sea level (Peng et al., 2013; Rong et al., 2007), surface winds
61 (Huynh et al., 2016), precipitation (Juneng and Tangang 2005; Nguyen et al., 2014; Räsänen
62 and Kumm, 2013; Räsänen et al., 2016), cyclone frequency occurrences (Camargo and
63 Sobel, 2005; Wu et al., 2005), and river runoff (Räsänen and Kumm, 2013; Xue et al., 2011).
64 Some of the aforementioned studies have focused further on the trends in the analyzed
65 variables, especially to estimate the potential impacts of global warming or decadal
66 variability (e.g., Peng et al., 2013; Xue et al., 2011).

67 As a complement to the large and growing body of regional climate-related
68 publications stemming from different authors, journal articles, datasets, and analyses of
69 specific time periods and time scales, the goal of the present study is to make an original
70 contribution to the literature by attempting to provide a concise and integrated analysis of
71 five key oceanic, atmospheric and terrestrial variables. To our knowledge, this study is
72 actually the first co-analysis of regional (SCS) oceanographic variables conducted over a



73 multi-decadal time frame made possible by the presence of long-term data products. For this
74 co-analysis, our approach is based on a coherent methodology, using the same technique for
75 each key variable, comparing each variable with the same ENSO indices, computing trends
76 over the same period, and using either new or longer datasets than the ones currently found
77 in the literature. Furthermore, this study provides an analysis of altimeter-derived Mekong
78 and Red Rivers discharge, which has not been previously documented, as well as in situ P
79 changes in near-coastal stations of Vietnam. The five key variables studied here are sea
80 surface temperature, sea level anomalies, surface winds, precipitation and river discharge,
81 all of which are considered an Essential Climate Variable (ECV) in the frame of the Global
82 Climate Observing Systems (GCOS, 2016). (In total, 50 variables covering three domains,
83 atmospheric, oceanic and terrestrial, are referenced as ECVs).

84 The five ECV datasets and the common data analysis methods based on temporal
85 filtering and EOF analysis are detailed in section 2. Their long-term means and standard
86 deviations (denoting the overall variability) are described in section 3 to set the context.
87 Then, their seasonal and interannual (ENSO) variabilities are analyzed in sections 4 and 5,
88 respectively. The long-term trends are finally documented in section 6. Aiming to be a short
89 overview paper, the knowledge gained from our study is compared to a variety of previous
90 results in all sections. A conclusion and discussion section is given in section 7.

91

92 **2. Data and Methods**

93 Five ECVs are investigated: sea surface temperature (SST), sea level anomaly (SLA),
94 surface wind (SW), precipitation (P) and water discharge (WD). Among the multiple
95 available databases, all of the products that are described next have been selected based on a
96 compromise between several criteria: the dataset is as long as possible, grid resolution must
97 be as fine as possible, confidence, robustness and/or 'clear' documentation of the product
98 (partly based on a literature review).



99 SST. The primary datasets we selected are the 1° daily optimum interpolation SST
100 (daily OISST) version 2.0 developed by the National Oceanic and Atmospheric
101 Administration (NOAA; Reynolds et al., 2007; Reynolds 2009). (Note that all websites we
102 used to get the data are listed in the Acknowledgements section below). We extracted the
103 merged and gridded SST data covering the SCS from 0-24°N to 100-120°E and spanning
104 from 01/1982 to 12/2015 (34 years).

105 SLA. We used the multi-mission gridded sea level anomaly (MSLA) product produced
106 by AVISO+ (Archiving, Validation and Interpretation of Satellite Oceanographic Data) that
107 was based on TOPEX/Poseidon, Jason 1, ERS-1 and ERS-2 data. This product provides SLAs
108 relative to a 20-year mean from 1993 to 2012. This weekly data set is averaged to produce
109 the monthly mean data set in the present work and covers the same area as the SST data
110 from 01/1993 to 12/2015 (23 years) with a resolution of 0.25°x0.25°. The mean dynamic
111 topography (called the CNES-CLS13 MDT) was also obtained from AVISO+ and gives the
112 surface height above geoid over the period 1993-2012 (Rio et al., 2014). This product is
113 based on two years of GOCE (Gravity Field and Steady-State Ocean Circulation Explorer)
114 data, seven years of GRACE (Gravity Recovery and Climate Experiment) data and 20 years of
115 altimetry and in situ data.

116 SW. To investigate the SW, we selected the 10-m ERA-Interim merged and gridded
117 wind data developed by the European Centre for Medium-Range Weather Forecasts
118 (ECMWF; Dee et al., 2011). The data are available monthly on a 0.75°x0.75° spatial grid
119 covering the entire region for the period 01/1979 to 12/2015 (37 years).

120 P. The ERA-Interim reanalysis is also used as a source of precipitation data with the
121 same resolution and time coverage as previously noted. To further the study of precipitation,
122 we selected to investigate the land rainfall measurements provided by Vietnam's Hydro-
123 Meteorological Service. Among the 172 rainfall stations available, only 17 are considered in
124 this study. The selection was made regarding the following criteria: a) the data set must



125 cover at least 28 consecutive years, b) the dataset should not contain any missing data, c) the
 126 spatial distribution must be homogeneous across Vietnam, and d) at least one station must
 127 be located in each of the eight climatic zones of Vietnam described in Gobin (2016). The
 128 locations and primary characteristics of the 17 selected rainfall stations are shown in Table
 129 1. The correlation coefficients (R) between the in situ and ERA-Interim reanalysis time series
 130 sampled near each station were high, and the values were similar for both seasonal and
 131 interannual time scales ($0.5 < R < 0.98$). However, the ERA-Interim product tended to
 132 underestimate the mean observed rainfall by approximately 16% (comparison made
 133 between the 17 selected stations). Only 3 times series representing the northern (Lục Yên),
 134 central (Đà Nẵng) and southern (Mỹ Tho) parts of Vietnam are presented in the following
 135 section.

Position	Name	Mean	Standard Deviation	Linear Trend
21°.22'N, 103°.00'E	Điện Biên	4.31	4.37	-2.4x10 ⁻¹
22°.06'N, 104°.43'E	Lục Yên	8.18	6.05	-2.64x10 ⁻¹
21°.10'N, 105°.03'E	Minh Đài	4.93	4.86	-7.8x10 ⁻¹
22°.50'N, 106°.31'E	Trùng Khánh	4.90	4.38	-1.53x10 ⁻¹
21°.01'N, 107°.21'E	Cửa Ông	4.97	5.73	-4.10x10 ⁻²
20°.39'N, 106°.03'E	Hưng Yên	3.94	3.80	7.42x10 ⁻⁴
19°.10'N, 105°.38'E	Quỳnh Lưu	4.37	4.49	-7.2x10 ⁻²
18°.05'N, 106°.17'E	Kỳ Anh	5.68	6.32	-4.71x10 ⁻¹
16°.80'N, 106°.60'E	Đông Hà	10.48	11.55	-5.20x10 ⁻¹
16°.02'N, 108°.12'E	Đà Nẵng	14.42	15.00	1.48
14°.46'N, 108°.44'E	Ba Tơ	7.12	9.36	7.42x10 ⁻¹
13°.03'N, 108°.59'E	Sơn Hoà	4.93	6.76	1.57x10 ⁻¹
11°.45'N, 108°.23'E	Liên Khương	7.98	6.22	8.12x10 ⁻¹
11°.50'N, 106°.59'E	Phước Long	6.78	5.78	3.53x10 ⁻¹
10°.47'N, 105°.56'E	Mộc Hoá	4.05	4.14	-1.08x10 ⁻¹
10°.21'N, 106°.24'E	Mỹ Tho	8.54	6.78	6.73x10 ⁻¹
9°.17'N, 105°.43'E	Bạc Liêu	5.85	5.37	6.45x10 ⁻⁴
ST (21°.20'N, 105°.50'E)	Sơn Tây	3540	2960	-520



CCV Satellites	Chroy Chang Var	12400	8280	-1220
CCV in situ (12°.50'N, 105°.65'E)	Chroy Chang Var	11600	10700	-1340

136 **Table 1.** Means, standard deviations and trends from the 17 selected inland rainfall stations
 137 in Vietnam (in mm/d and mm/decade), and the Red River ST, Mekong CCV in situ WD
 138 stations and CCV from satellite measurements (in m³/s and m³/s/decade), along with their
 139 coordinates. The values were computed over the 1979-2006 period for the rainfall stations,
 140 over the 1960-2010 period for the ST gauge station, over the 1960-2002 period for the in
 141 situ measurements at CCV and over the 1996-2015 period for CCV from satellite
 142 measurements.

143 WD. Finally, two river systems are considered in this study: the Red River and the
 144 Mekong River, which are represented by the Son Tay (ST) station and the Chroy Chang Var
 145 (CCV) station (located in Cambodia), respectively (see Fig 3e for locations). The latter station
 146 was selected to avoid the tidal effects on the water level in the Mekong Delta. In situ data are
 147 available at the ST and CCV stations, and water discharges were further computed from
 148 altimetry at the CCV station. Radar altimetry discharges were obtained applying a rating
 149 curve that related the water stage and discharge to the altimetry-based water level (e.g.,
 150 Kouraev et al., 2004; Frappart et al., 2015). The time-series of altimetry-based water levels
 151 was obtained using the Multi-Mission Altimetry Processing Software (MAPS – Frappart et al.,
 152 2015) to process the along-track altimetry data from ERS-2 (1996-2003), ENVISAT (2002-
 153 2010 on the nominal orbit) and Jason-2 (2008-2016 on the nominal orbit). The data, made
 154 available by the Centre de Topographie des Océans et de l'Hydrosphère (CTOH), came from
 155 the Geophysical Data Records (GDRs) D for Jason-2 and v2.1 for ENVISAT and from the
 156 reprocessing of the ERS-2 radar echoes performed at CTOH to ensure the continuity with
 157 ENVISAT for land studies (Frappart et al., 2016). In situ data at the ST station are provided
 158 by Vietnam's Hydro-Meteorological Service and cover the period 1960 to 2010. The data
 159 from the CCV station are from the Mekong River Commission and cover the period 1960 to



160 2002. The mean annual discharges from the gauge stations at the CCV station were
161 compared to the satellite data over the common period of measurements, 1996 to 2002. It
162 appeared that the annual means of the in situ measurements were adequately represented
163 by the satellite measurements since the slope of the regression line (between in situ and
164 satellite measurements) is close to one.

165 Climate indices. The interannual signal that was extracted from the original time
166 series (see the following paragraph) was compared to several well-known climate indices to
167 search for possible relationships with the atmospheric El Niño Southern Oscillation (ENSO)
168 Index (SOI) (Allan et al., 1996), the oceanic ENSO indices through the SST Niño3.4 (5°S-5°N,
169 170°W-120°W), SST Niño4 (5°S-5°N, 160°E-150°E) and SST Niño1+2 (10°S-0°, 90°W-80°W)
170 indices (Trenberth and Stepaniak, 2001 Rayner et al., 2003), and the El Niño Modoki index
171 (EMI) (Ashok et al., 2007). The SST Niño1+2 index is preferentially used to characterize
172 Eastern Pacific (EP) ENSO events. The SST Niño4 index is preferentially used to characterize
173 all types of El Niño events, but the authors could have chosen to use either the SOI or the SST
174 Niño3.4, as the phases of these three indices are almost equally sensitive to El Niño events
175 (Hanley et al., 2003).

176 Data processing. The climatological means, standard deviations (STDs), seasonal and
177 interannual variations were quantified for each ECV. The climatological means and STDs
178 were calculated over the entire length of each dataset (ranging from 23 to 37 years). The
179 seasonal variations were estimated by constructing a typical year for each ECV. This method
180 consists of computing the mean of each month (J, F, ..., D) of the year over the multiyear
181 series. The interannual variations were estimated by subtracting the typical year from the
182 original series, which removes the mean seasonal cycle and filtering the remaining signal
183 with a 13-month low-pass Hanning filter. The filter passes almost no signals at periods less
184 than or equal to six months, filtering out the intraseasonal variability, and shortens each
185 time series by 6 months at the two extremities. Empirical orthogonal function (EOF)



186 analyses were then performed on the typical years and low-pass filtered time series, which
187 were first detrended. EOF analyses allow us to extract the main spatial modes of variability
188 and determine how they can change over time (e.g., Hannachi et al., 2007). Only statistically
189 consistent EOFs, based on North et al. (1982), are shown here, and all of the values
190 presented below are significant at the 90% confidence level (except for the P and WD
191 stations, as we did not perform EOFs on these series). Although statistically significant, some
192 EOF modes equal to or greater than two are not presented below because we did not find
193 any simple physical mechanisms possibly accounting for their related temporal and spatial
194 functions.

195 The long-term trends were computed by least-square fitting a straight line to the
196 monthly time series over the entire length of each dataset. The long-term trends over a
197 common period of measurement of 27 years (1979-2006) are also calculated and presented
198 when available (for P and SW from Era-Interim, P in situ and WD at ST).

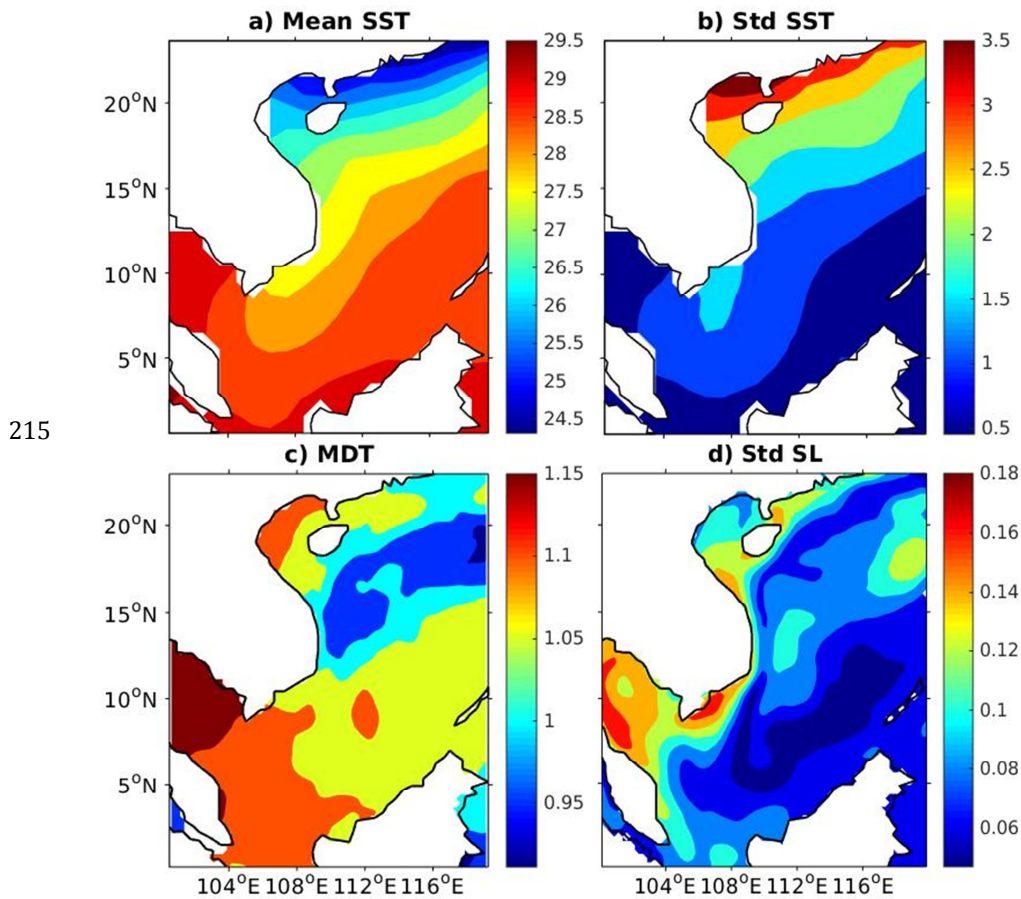
199 **3. ECV means and standard deviations**

200 The mean and standard deviation are presented for each oceanic and atmospheric
201 variable in Figures 2 and 3, respectively, and the atmospheric variables are available over
202 both the ocean and continent.

203 SST. The mean SST ranges from 24.5 to 29.5°C with the lowest values in the northern
204 part of the SCS basin and along the coasts of Vietnam (Fig. 2a), in agreement with Tuen
205 (1994), Chu et al. (1997) and Qu (2001) to name a few. Liu et al. (2004) also emphasized a
206 (relatively) cold tongue of water as the result of the advection of cold waters from the north
207 via the western part of the cyclonic gyre that develops in the winter in the area. The
208 standard deviation (Fig. 2b) ranges from 0.5 to 3.5°C with a high variability in the northern
209 part of the basin. On both the mean and standard deviation maps, the northeast-southwest
210 oriented isotherms are observed to have low temperatures and high standard deviations in
211 the north-northwest (see also Chu et al., 1997, and Qu, 2001). The lowest SSTs are mainly



212 caused by the northeast winds that blow in the winter, which first cool the seawater by
213 bringing cold and dry air and second generate a southwest-ward coastal current, which, in
214 return, brings cold coastal waters from the East China Sea into the SCS (Fang et al., 2006).



216
217 **Figure 2.** Mean and standard deviation of SST (a and b, respectively) in °C, and mean
218 dynamical topography (MDT) and standard deviation of SLA (c and d, respectively) in m. The
219 values were computed over 1982-2015 for SST, and 1993-2012 for MDT. The color codes
220 differ between the figures.

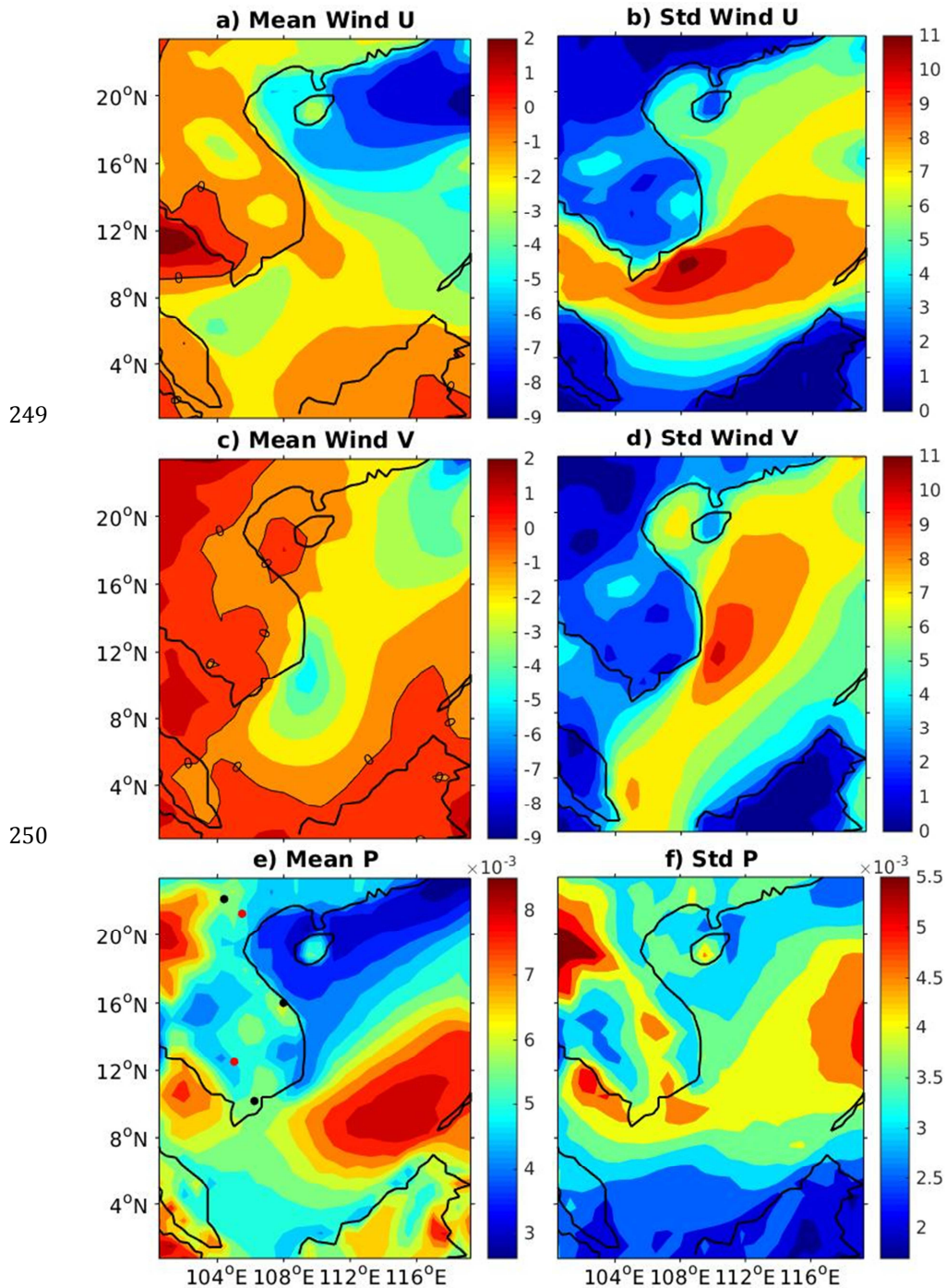
221

222 SLA. The map of the mean dynamic topography (MDT) shows spatial inhomogeneity
223 throughout the basin, featuring the mean surface geostrophic circulation (Fig. 2c). The
224 western and the southwestern parts of the SCS are characterized by the highest rates of



225 MDT, ranging from 1.05 to 1.15 m above the reference geoid. The lowest sea surface heights,
226 with values ranging from 0.9 to 1 m, stretch roughly from the southern tip of Vietnam to the
227 Luzon Strait, with minimum values near 18°N-118°E and 14°N-110°E. Zhuang et al. (2010)
228 found similarly low sea level heights at approximately 18°N-117°E northwest of Luzon
229 Island that extended southeastward to the east of Vietnam. Interestingly, the MDT resembles
230 the mean 0/400dbar dynamic topography derived from in situ temperature profiles and
231 mean TS curves (Qu, 2000). This similarity corroborates the existence of the cyclonic West
232 Luzon and East Vietnam eddies, which are two major features of the mean upper circulation
233 that are centered at the minimum values noted above. The SLA standard deviations range
234 from 6 to 18 cm (Fig. 2d), which is consistent with the results from Zhuang et al. (2010).
235 These results are comparable with previous results from TOPEX/Poseidon altimeter data
236 and Argo-tracked ocean surface drifter measurements presented by Ho et al. (2000).

237 SW. The mean surface zonal and meridional components are stronger over the sea
238 than over the land area, and the winds mostly blow W-SW (negative values in Fig. 3ac),
239 particularly in the northern part of the basin where the values are as high as 8.5 m/s
240 (approximately 16.5 knots). A mean southward flux is observed along the south of the
241 Vietnamese coastline. It appears that the mean surface winds and the standard deviations
242 associated with both zonal and meridional winds strongly depend upon the orographic
243 features (lower values above lands). The interpretation of the annual mean surface wind in a
244 region that is highly influenced by strong seasonal wind reversals due to the monsoon cycles
245 (see section 4) does not mean very much. The standard deviation values are the lowest
246 above land (from 0.5 to 4 m/s) and the highest above water (from 5 to 11 m/s) with cores of
247 maximum values near the southern tip of Vietnam. These values mostly reflect the seasonal
248 reversal (chiefly over the ocean) of the wind driven by the summer-winter monsoon cycles.



252 **Figure 3.** Means (a, c, e) and standard deviations (b, d, f) of the zonal and meridional surface
253 wind components in m/s (noted U and V, respectively) and precipitation in m/d (noted P).

254 Positive U and V wind components are directed to the East and the North, respectively. The
Page 13 of 48



255 black dots on panel (e) denote, from north to south, the location of the inland rainfall
256 stations Lục Yên, Đà Nẵng and Mỹ Tho (see Table 1). The red dots denote the location, from
257 north to south, of the gauge stations at the Red River ST and Mekong CCV stations. The color
258 codes differ between the figures.

259 P. The south-central part of the SCS basin hosts the maximum P rate of approximately
260 8 mm/d. The lowest mean P rates are observed in the northern part of the basin and along
261 the Chinese coastline (Fig. 3e). As discussed in Wang et al. (2009), the sharp P contrast
262 between the NW and SE parts of the SCS arises from a similar SST contrast (see Fig. 2a). The
263 standard deviation of P ranges from 1.5 to 5.5 mm/d (Fig. 3f). The rainfalls data from in situ
264 measurements at 17 Vietnam stations (Table 1) range from 8.2 to 14.4 mm/d
265 (corresponding to approximately 3 to 5.3 m/yr). These measurements are consistent with
266 the results from Gobin et al. (2016) who noted that rainfall on land was measured within a
267 range of approximately 0.65 m/yr to more than 7.3 m/yr for the period 1960-2009. Here,
268 the mean rainfall for the in situ stations that were considered is approximately 3.8 m/yr
269 with the highest rate in the central part (Da Nang), as found in Gobin (2016). The standard
270 deviations range from 6.05 to 15 mm/d.

271 WD. At the ST Red River River station, the mean water discharge is equal to 3540
272 m³/s (for the period 1960 to 2010) with a standard deviation of approximately 2960 m³/s,
273 which is similar to the results from Vinh et al. (2014). At the CCV Mekong station, the mean
274 water discharge from the gauge stations and satellites appear to be consistent (11600 and
275 12400 m³/s, respectively).

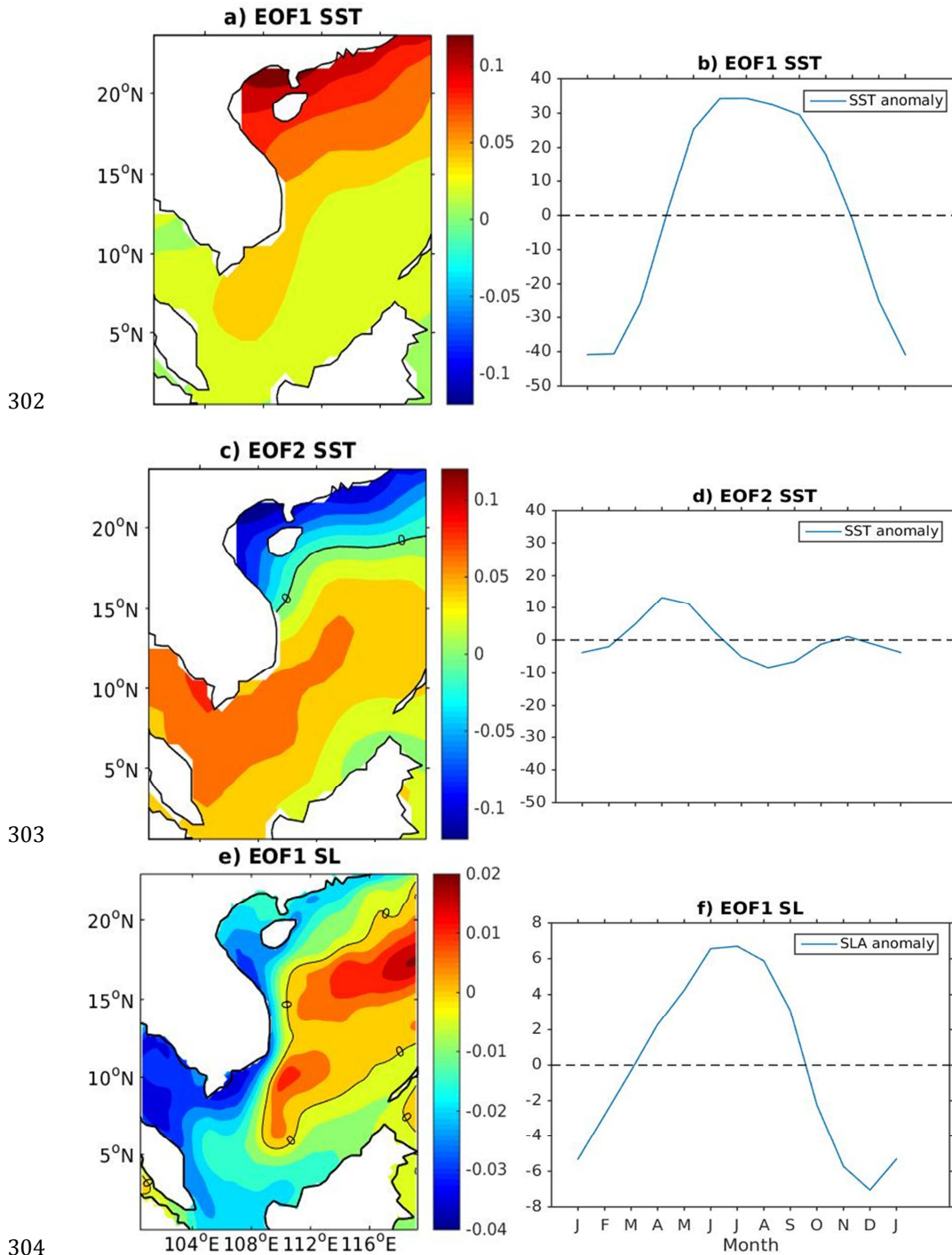
276 **4. Seasonal variability**

277 SST. The first seasonal EOF mode on SST (94% of the total variance) represents an
278 annual cycle (Fig. 4b). The spatial function is positive over the entire basin and high in the
279 northwestern part of the basin and along the southeastern Vietnam coast (Fig. 4a). The
280 temporal mode reaches troughs in January-December and peaks in June-July, and they



281 correspond to the cold northeast winter monsoon and the warm southwest summer
282 monsoon, respectively. Thus, compared to the mean, this mode exhibits a cooling (up to -
283 4.8°C) over the entire basin in the winter and a warming (up to 4.2°C) mainly in the
284 northwest in the summer.

285 The second seasonal EOF mode (5% of the total variance) represents a semi-annual
286 cycle with peaks in April and November and troughs in January and August (Fig. 4d). The
287 spatial function is positive over the majority of the basin and negative along the Chinese and
288 northern Vietnamese coasts (Fig. 4c). In April, the SST can increase by as much as 1.5°C in
289 the Gulf of Thailand and south of Vietnam, and can decrease by -1.5°C in the Gulf of Tonkin.
290 As noted by Huynh et al. (2016), this semi-annual variability is mostly driven by oceanic
291 thermal advection along the northeast-southwest diagonal of the basin from two opposite
292 directions. These authors partially associate the spatial and temporal variabilities of the
293 second SST mode with the influence of an atmospheric anticyclone. In late March, the strong
294 development of this anticyclone weakens the northeast monsoon (winter monsoon), which
295 reduces the amount of clouds and rainfall over the SCS and allows more solar radiation to
296 reach the basin. As a result, the SST increases and reaches its peak in April and provides heat
297 and vapor for the onset of the southwest (summer) monsoon. The southwest winds trigger
298 the development of an anticyclone in the south and a weaker cyclone in the north, leading to
299 the advection of warm waters from the south to the northeast and cold waters from the
300 north to the southwest. In October, the summer monsoon dissipates and allows solar
301 radiation to warm the basin, reaching a peak in November.

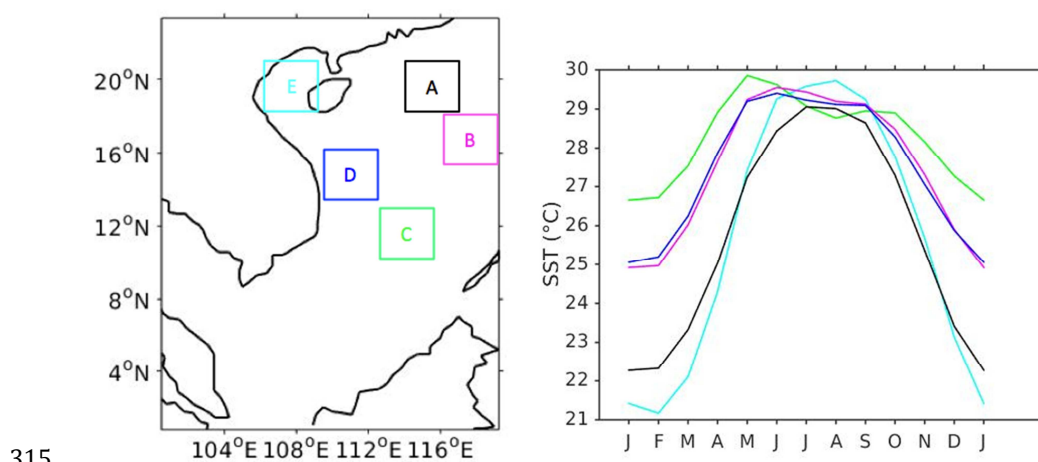


305 **Figure 4.** Spatial functions (a, c, e) and associated temporal functions (b, d, f) of the first and
306 second (only for SST) EOF seasonal modes of SST and SLA. The products between spatial and



307 temporal functions denote anomalous SST (in °C) and SLA (in m) respective to the mean
308 values.

309 To further analyze the SST seasonal changes, typical years are represented in four
310 boxes, following the criteria of Qu (2001) based on mixed layer depths (boxes A to D in Fig.
311 5). A fifth box (E) was added to represent the region of high variability in the Gulf of Tonkin.
312 The results correspond to those of Qu and highlight the main influence of monsoon cycles on
313 SST in boxes A and E, while box C (and B and D to a lesser extent) also seems to be
314 influenced by the thermal advection described above.



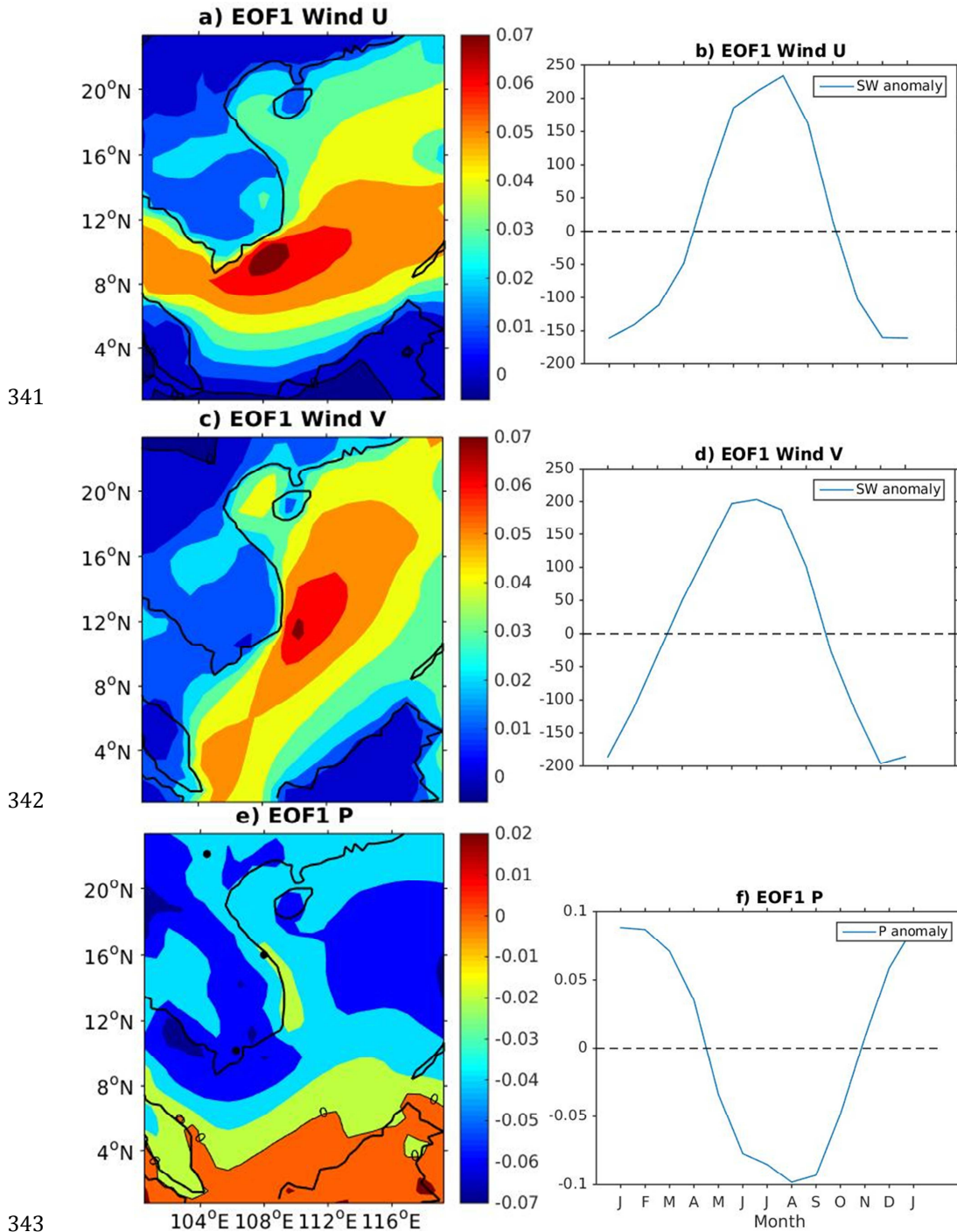
315
316 **Figure 5.** Locations of boxes (left) and time series of the relative SST monthly means (in °C)
317 over boxes A (black), B (magenta), C (green), D (blue) and E (cyan).

318 SLA. The first seasonal EOF mode on SLA accounts for 80% of the total variance of the
319 signal (Fig. 4ef). The spatial function shows positive values in the central and eastern parts
320 of the SCS and negative values in the western part of the basin. The temporal function
321 reveals higher-than-average (up to 0.14 m) SLAs in the summer in most of the basin and
322 lower-than-average SLAs along the coastlines of Vietnam, Cambodia and Malaysia. In the
323 winter, the situation reverses leading to negative anomalies over most of the basin and
324 positive anomalies along the coasts. Interestingly, this EOF mode also emphasizes lower-
325 than-average SLA in the winter near the center of the West Luzon eddy (as well as the East



326 Vietnam eddy, although to a lesser extent). Logically, the timing of those seasonal SLA drops
327 corresponds to the maximum development of the two eddies inferred from hydrographic
328 observations (Qu, 2001). In addition, the seasonal sea level drops that are observed in the
329 summer along the coasts are consistent with the upwelling-favorable surface winds that
330 blow to the northwest at that time of the year (see below).

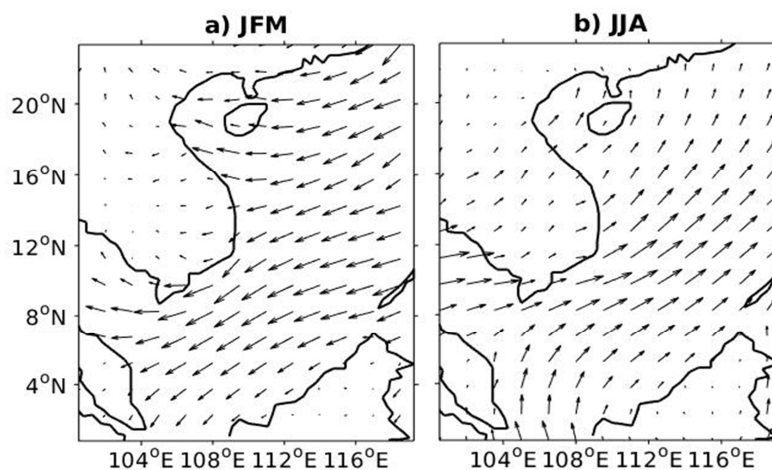
331 SW. The first seasonal EOF mode on surface wind anomalies contributes to up to 93%
332 of the variance for both zonal (U) and meridional (V) components. The two temporal
333 functions show an annual cycle, and the spatial functions show positive values over the
334 entire region and more intense values over the sea (Fig. 6a-d). In the summer, the eastward
335 (U) and northward (V) anomalies are then more intense (up to 17 m/s). The situation
336 reverses in the winter with negative anomalies up to 10 m/s. The January-February-March
337 (JFM) and June-July-August (JJA) mean wind vectors are shown in Figure 7, which stress the
338 seasonal monsoon reversal to ease the interpretation of the EOF analysis performed
339 separately on each wind component. The wind anomalies strongly depend upon the
340 orographic features of the region: the seasonal wind anomalies are stronger above the sea.



344 **Figure 6.** Spatial functions (a, c, e) and associated temporal functions (b, d, f) of the first
 345 seasonal EOF modes on the U and V components of the surface wind, and P. The products
 346 between the spatial and temporal functions denote anomalous U and V (in m/s) and P (in



347 m/d) respective to the mean values. The black dots in Figure 6e are the same as those in
348 Figure 3e.



349

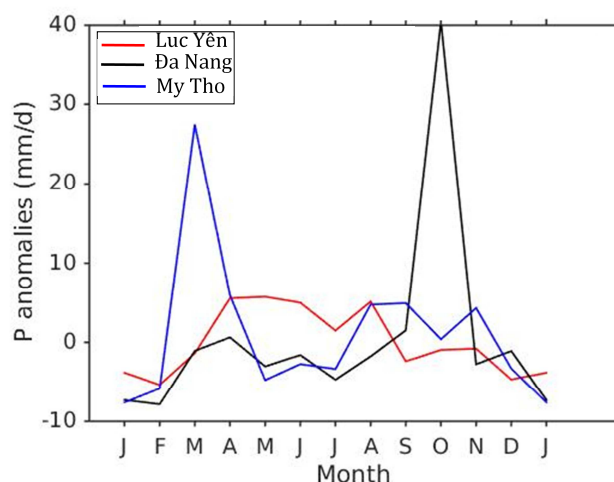
350 **Figure 7.** Mean surface wind in January-February-March (a) and June-July-August (b). The
351 arrows denote the wind vectors, and the longest arrows equal 8 m/s.

352 P. The first seasonal EOF mode on P contributes to 69% of the total variance (Fig.
353 6ef). A clear annual cycle appears on the temporal function. North of 8°N during the summer,
354 the entire region undergoes positive rainfall anomalies as intense as 6 mm/d, except along
355 the central coastline of Vietnam where the anomalies are slightly lower, which possibly
356 corresponds to the upwelling-favorable wind effects and relatively cold SST patterns near
357 the coast (Chu et al., 1997). During the winter, the signs of the anomalies reverse and the
358 region north of 8°N undergoes seasonal rainfall deficits compared to the mean.

359 The seasonal P anomalies relative to the means (see values in Table 1) of the three
360 selected in situ stations are shown in Figure 8. The anomalous values can be as high as 40
361 mm/d and as low as -8 mm/d, with a tendency to depict annual, Dirac-like, and semi-annual
362 functions at the Lục Yên, Đà Nẵng and Mỹ Tho stations, respectively. The results for the Lục
363 Yên station and the peak observed in the autumn at the Đà Nẵng station are qualitatively
364 similar to the observations (from different periods) by Nguyen et al. (2014). The authors



365 emphasize that the months of peak rainfall coincide with the southward migration of the
366 subtropical ridge and the intertropical convergence zone.



367

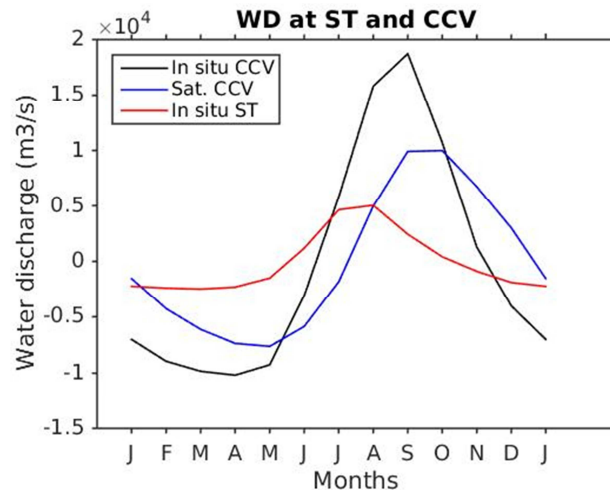
368 **Figure 8.** Seasonal variability of precipitation anomalies relative to the means from in situ
369 land stations, Lạc Yên (red), Đà Nẵng (black) and Mỹ Tho (blue). The station locations are
370 denoted by black dots in Figures 3e and 6e (see also Table 1). The units are in mm/d.

371 WD. Figure 9 presents the seasonal variability relative to the means (see values in
372 Table 1) of the water discharge from the Red River (at ST) and Mekong River (at CCV). The
373 discharges observed at the ST station (red line) are much lower than those at the CCV station
374 (black and blue lines), with anomalies ranging from -1.10^4 to $+2.10^4$ m³/s. At the CCV station,
375 the highest discharge flux is observed in September (from both gauge station and satellite
376 measurements) with anomalies as high as 1.8×10^4 and 1×10^4 m³/s for the in situ and
377 satellite data, respectively. The entire water discharge series shows a peak in the summer
378 and a trough in the winter. This variability is probably driven by the monsoon dynamics
379 with a peak in water flow during the rainy season (summer monsoon) and negative
380 anomalies during the dry season (winter monsoon), as illustrated in Figures 6ef and
381 discussed above.

382 To explain the different amplitudes between the satellite and gauge station data at the
383 CCV Red River station (black and blue lines in Fig. 9), measurements over the common



384 period (1996-2002) were compared (not shown here). Both in situ and satellite
 385 measurements showed similar amplitudes although the satellite measurements showed 1-2-
 386 month lags in the peak and trough, for currently unknown reasons.



387

388 **Figure 9.** Seasonal variability of the water discharge (WD) anomalies relative to the means
 389 at the (Red River) ST station from gauge station measurements (period: 1960-2010) in red,
 390 and at the (Mekong River) CCV station from gauge station measurements (period: 1960-
 391 2002, in black) and satellite measurements (period 1996-2015) in blue. The units are in 10⁴
 392 m³/s. The mean values are reported in Table 1.

393 5. Interannual variability

394 As noted in section 2, EOF analyses are performed to extract the main interannual
 395 variability and compare with ENSO indices. The maximum correlation coefficients at given
 396 lags between the interannual temporal function of the EOF and all (low-pass filtered) climate
 397 indices are listed in Table 2.

Time series	R (lag in months)				
	Niño1+2	Niño3.4	Niño4	SOI	EMI
SST EOF1	0.59(6)	0.45(6)	-0.38(-12)	-0.44(-5)	-0.40(12)
SST EOF2	0.22(12)	0.58(0)	-0.55(2)	0.55(1)	-0.53(2)
SLA EOF 1	0.34(0)	0.70(2)	0.78(3)	-0.74(2)	0.62(4)
SW U EOF1	-0.51(3)	-0.69(4)	-0.64(5)	0.65(5)	-0.42(7)
SW V EOF 1	0.60(0)	0.74(2)	0.58(3)	-0.71(3)	0.28(4)
P EOF1	0.25(0)	0.57(0)	0.64(0)	-0.60(0)	0.49(2)



398 **Table 2.** Maximum correlation coefficients (R) at given lags (given in months in brackets)
399 between the ENSO indices and reported interannual EOF time functions (as shown in Figs.
400 11 and 13). A positive lag indicates that the indices lead the variable. All R values are
401 significant at the 90% confidence level.

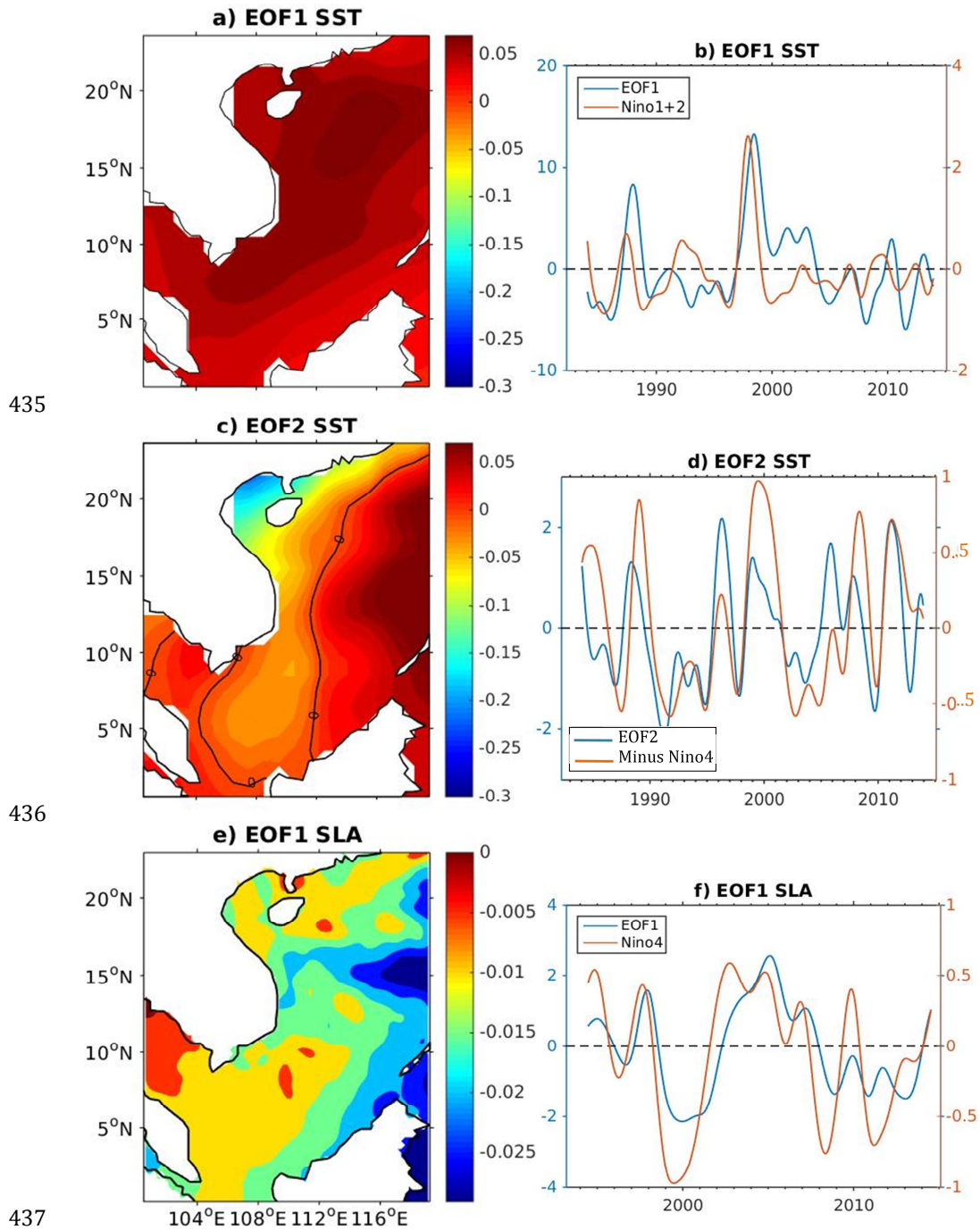
402 SST. The spatial pattern of the first interannual EOF mode on SST (75.4% of the total
403 variance) is positive over the entire SCS with highest values along a northeast-southwest
404 diagonal (Fig. 10a). The associated temporal function (Fig. 10b) shows a maximum
405 correlation coefficient value of +0.59 with the Niño1+2 index (Table 2) with an index lead of
406 6 months. Thus, it appears that 6 months after the mature phase of an Eastern Pacific El Niño
407 event (represented by the Niño1+2 index, see section 2), a basin-wide SCS peak warming of
408 SST occurs. This peak is especially clear during the strong events of 1986-87 and 1997-98
409 when the SST increased by up to 0.7 and 1.0°C, respectively, in the central northern parts of
410 the SCS.

411 The spatial pattern, the anomalous amplitude and the lag are quite similar to those of
412 Chu et al. (1997) and Fang et al. (2006) that were obtained from different data sets and time
413 periods. They further resemble the averaged February and August double-peak structures of
414 the SCS SST composite anomalies derived from seven El Niño events covering 1950-2002 by
415 Wang et al. (2006). The lagging response of SST to ENSO events (observed here for Niño1+2,
416 and in Table 2 for Niño3.4, Niño4 and EMI) is described as a common feature in tropical
417 oceans. Klein et al. (1999) and Wang et al. (2004) attribute this lag to the effect of the
418 atmospheric bridge and the thermal inertia of the ocean mixed layer in the tropical Pacific.

419 The second interannual EOF mode on SST (7.3% of the variance) is represented by
420 positive spatial values in the SCS except near the Chinese and Vietnamese coasts and south
421 of Vietnam (Fig. 10c). The temporal function is best correlated to both the SOI and the Niño4
422 index (R= -0.55) with lags of one and two months, respectively, which are considered to be
423 representative of all types of ENSO events. Superimposed over the overall SST warming



424 during the strong EP-type El Niño events depicted in the first EOF mode, it indicates that all
425 El Niño events produced SST decreases of approximately 0.1°C in the eastern half of the
426 basin and SST increases of up to 0.2°C along the coasts and south of Vietnam. The La Niña
427 events, not clearly visible in the first EOF mode (as in Wang et al., 2006), led to an SST
428 increase in most of the SCS, except along the coast and south of Vietnam where the
429 temperatures decreased. The first interannual EOF mode on the wind stress curl (not shown
430 here), an alias for Ekman pumping, represents 40% of the total variance, and the related
431 time function is correlated with the Niño4 index ($R=0.6$). Interestingly, its spatial pattern
432 proves rather consistent with the second interannual EOF mode on SST, being favorable to
433 upwelling (downwelling) in the eastern (western) half of the basin during El Niño (and vice
434 versa for La Niña).



438 **Figure 10.** Spatial functions (a, c, e) and associated temporal functions (b, d, f) of the first
 439 and second interannual (only for SST) EOF modes on SST and SLA. The products between
 440 the spatial and temporal functions denote anomalous SSTs (in °C) and SLAs (in m),



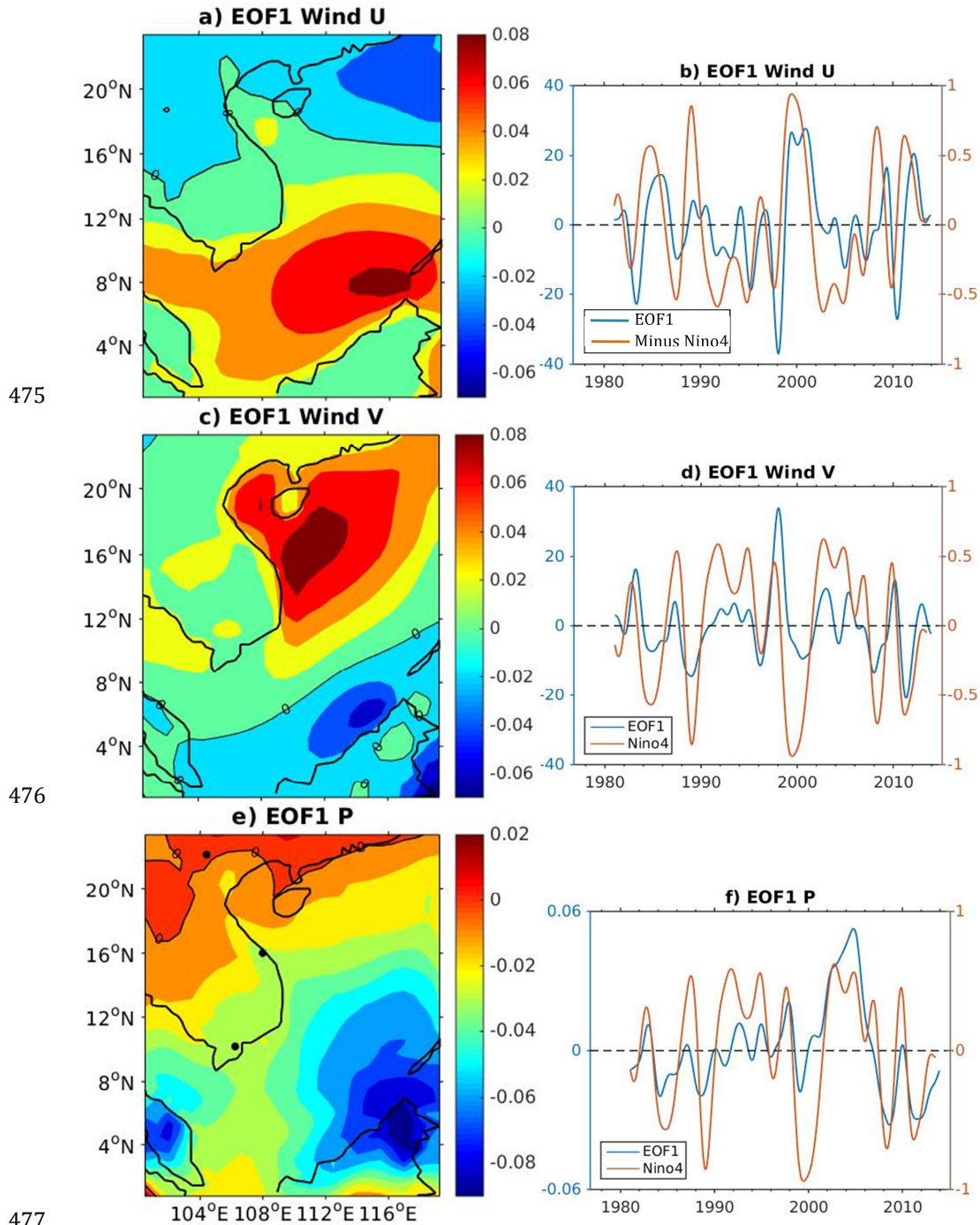
441 respective to the mean values. The Niño1+2 (b, in blue) and the Niño4 SST indices (d, f, in
442 red) are plotted over the time functions. The Niño4 index is reversed on panel (d). For
443 clarity, the temporal functions and the indices are filtered again with the H25 filter but are
444 described in the text with the TY-H13 filtration method.

445 SLA. Figure 10ef displays the first interannual EOF mode on the SLA, which accounts
446 for 48.1% of the total variance. The spatial patterns of this EOF mode are characterized by
447 the same negative sign throughout the basin (but with large horizontal gradients in
448 amplitude), which indicates that SLAs occur consistently over the entire SCS. The associated
449 temporal function is highly correlated ($R=+0.78$; lag=3 months) with the Niño4 index (Table
450 2). This EOF mode reveals that the sea level drop is largest three months after the mature
451 phase of an El Niño event. The negative SLA can be as strong as 5-10 cm in the eastern part
452 of the basin and along approximately 15°N . A reverse situation occurs during a La Niña year.
453 Rong et al. (2007) found similar spatial and temporal patterns for the period 1993-2005
454 with high correlation with the SOI (the only index tested). The observed anomalies are
455 consistent with the results presented by Fang et al. (2006) based on 1993-2003 satellite
456 altimetry data and with the results from a data assimilation model ran for the period 1993-
457 2002 (Wu and Chang, 2005).

458 SW. The first interannual EOF mode on zonal wind contributes to 64% of the total
459 variance of the signal (Fig. 11ab). The spatial function is positive in the southern part of the
460 region and negative north of approximately 14°N . The temporal function shows a high
461 negative correlation of $R=-0.64$ (Table 2) with the Niño4 index leading by five months (and
462 $R=-0.69$ with Niño3.4 leading by 4 months). This result indicates that 4-5 months after the
463 mature phase of an El Niño event, the eastward winds reach their maximal weakening (up to
464 -4 m/s) south of 14°N and get stronger (up to 4 m/s) north of 14°N . The situation reverses
465 during La Niña phases.



466 The first interannual EOF mode on meridional wind explains 49.4% of the total
467 variance with a positive spatial pattern north of approximately 6°N (Fig. 11c). The
468 corresponding temporal function is correlated with the SOI ($R=-0.71$) and the Niño3.4 index
469 ($R=+0.74$), with indices leading by 2-3 months. All types of El Niño events trigger an increase
470 in northward winds (e.g., up to 4 m/s during the 1997-98 event) north of 6°N and a decrease
471 of the same amplitude south of 6°N. These ENSO-related surface wind anomalies are
472 consistent with the results obtained by Wang et al. (2006) that were based on a composite
473 analysis, and those by Cheng et al. (2016) that were based on an EOF analysis, both obtained
474 from different wind field products and (shorter) time periods.



475

476

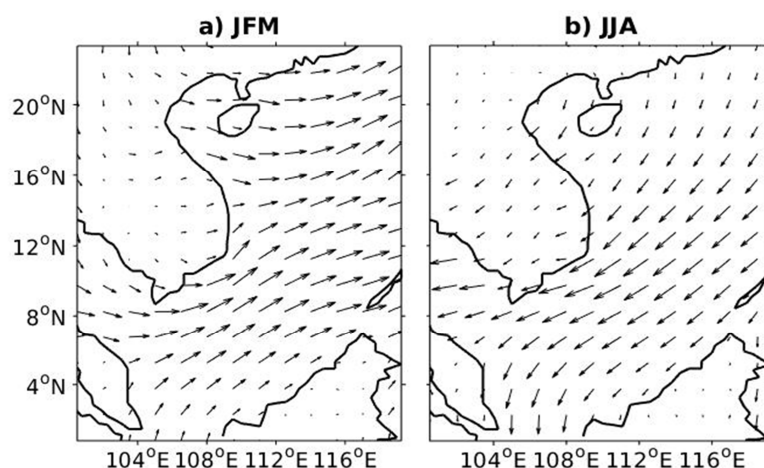
477

478 **Figure 11.** Spatial functions (a, c, e) and associated temporal functions (b, d, f) of the first
 479 interannual EOF modes on the U and V wind components and P. The products between the
 480 spatial and temporal functions denote anomalous winds (in m/s) and P (in mm/d),



481 respective to the mean values. The Niño4 SST index is plotted over the time functions. The
482 Niño4 index is reversed on panel (b). For clarity, the temporal functions and the indices are
483 filtered again with the H25 filter here but are described in the text with the TY-H13 filtration
484 method. The black dots in Figure 11e are the same as those in Figure 3e.

485 Figure 12 represents the composites of the anomalous wind vectors for the winter
486 during four strong El Niño events, noted JFM, and for the following summer, noted JJA. The
487 four El Niño events considered here are the 1982-83, 1986-87, 1991-92, and 1997-98
488 events, which were selected according to the studies of Chiodi and Harrison (2010, 2013).
489 The authors identified the abovementioned El Niño events as strong events that were
490 characterized by strong peaks in both Niño3.4 SST and outgoing long-wave radiation (OLR)
491 anomalies over the eastern-central equatorial Pacific. Figure 12a shows that the anomalous
492 winds were blowing N-NE, and when compared to the mean conditions in JFM when the
493 winds blow S-SW (Fig. 7a), this potentially leads to a weakened winter monsoon. The
494 anomalous JJA composites (Fig. 12b) show anomalous winds blowing S-SW, compared to the
495 mean conditions in JJA (when the winds blow N-NE (Fig. 7b)). Furthermore, each JFM and JJA
496 of each strong El Niño year were tested separately (not shown here), and the results showed
497 the same wind patterns as the JFM and JJA composites. Figure 12 compares the anomalies
498 over three months of a composite of strong El Niño events and is thus not directly
499 comparable with Figure 11abcd where the anomalies are presented relative to the long-term
500 mean, comprising all types of El Niño and La Niña events. Lastly, the same analyses were
501 performed on four La Niña years (1983-84, 1988-89, 1995-96, 1998-99). The surface winds
502 showed almost reversed patterns from the ones observed for El Niño years (not shown
503 here). The anomalous JFM composites for La Niña events showed anomalous wind blowing
504 S-SW, and the anomalous JJA composites showed anomalous wind blowing N-NE.



505

506 **Figure 12.** El Niño composites of the anomalous surface wind vectors in JFM (a) and JJA (b)
507 computed for 1983, 1987, 1992, and 1998, representing the 1982-83, 1986-87, 1991-92, and
508 1997-98 El Niño events, respectively. The arrows denote the vectors, with the longest
509 arrows equal to 1 m/s.

510 P. The spatial function of the first interannual EOF mode on P (48.4% of the total
511 variance) is negative over most of the region, except north of Vietnam, Laos and along the
512 Chinese coast, and it shows maximum values in the southeastern part of the region (Fig.
513 11e). The temporal function that is correlated with the Niño4 index ($R=0.64$ at 0 lag) reveals
514 that precipitation decreases during El Niño events and increases during La Niña phases. For
515 the case of the 1997-98 event, which was one of the strongest ENSO events ever recorded,
516 the amount of rainfall associated with EOF 1 (again representing only 48.4% of the variance)
517 reduces by as much as 1.6 mm/d in the southeast region, which is a reduction of 28%
518 relative to the mean value (Fig. 3f). The important P decreasing rate that was observed can
519 be explained by the eastward shift in convective activity in the equatorial western Pacific
520 during El Niño phases. Such shift leads to altered Walker circulation, generating a
521 subsidence area over the SCS (Wang et al., 2006).

522 From the 17 Vietnam rainfall stations tested, it appears that the linkage of
523 precipitation anomalies to ENSO is stronger at lower latitudes, with correlation coefficients



524 with Niño3.4 ranging from $R=-0.19$ to -0.45 . As an example, at station Đà Nẵng where $R=-$
525 0.45 , the rainfall decreases during El Niño phases by up to 4 mm/d during the 1997-98 El
526 Niño event (which is 70% of the mean). Nguyen (2014) also demonstrated that temperature
527 and rainfall variability are more strongly linked to ENSO events at lower latitudes of Vietnam
528 for the period 1971-2010. A study of the gridded precipitation data over the mainland of
529 Southeast Asia (1980-2013) that was undertaken by Räsänen et al. (2016) confirmed the
530 stronger influence of ENSO in the southern parts of the study area with high correlation to
531 ENSO during the spring of the decaying year.

532 WD. No obvious correlation was found between the interannual water discharge at
533 the ST Red River station and ENSO indices when the period 1960-2010 was considered.
534 However, when examining the period prior to the Hoa Binh Dam impoundment (from 1960
535 to 1978), the signal shows a statistically significant correlation to Niño4 ($R=-0.47$ at 12-
536 month lag). This suggests that the dam, by regulating the water flow according to the
537 dry/wet seasons and demand, may interfere with the interannual signal. At the CCV Mekong
538 station, both the 1960-2002 in situ and 1996-2002 satellite anomalies are correlated with
539 the SOI (+0.51 and +0.53, respectively, with an SOI lead of 6 months) and with the Niño4
540 index (-0.42 and -0.50 with 7-8-month lags, respectively). As an example, when considering
541 the 1997-98 event, the water discharge is reduced by approximately 4000 m³/s (i.e., 34% of
542 the mean) approximately 7 to 8 months after the event. Xue et al. (2011) showed a similar
543 connection between ENSO and Mekong runoff (at Pakse, Laos, approximately 400 km
544 upstream of the CCV station) for the period from 1993-2005. It is important to consider the
545 WD data with caution as the precipitation anomalies over the entire Red River and Mekong
546 River watersheds (143,000 and 795,000 km², respectively) are integrated and may relate
547 processes that occur outside of the area considered here and potentially far away from any
548 ENSO influence.

549 **6. Trends**



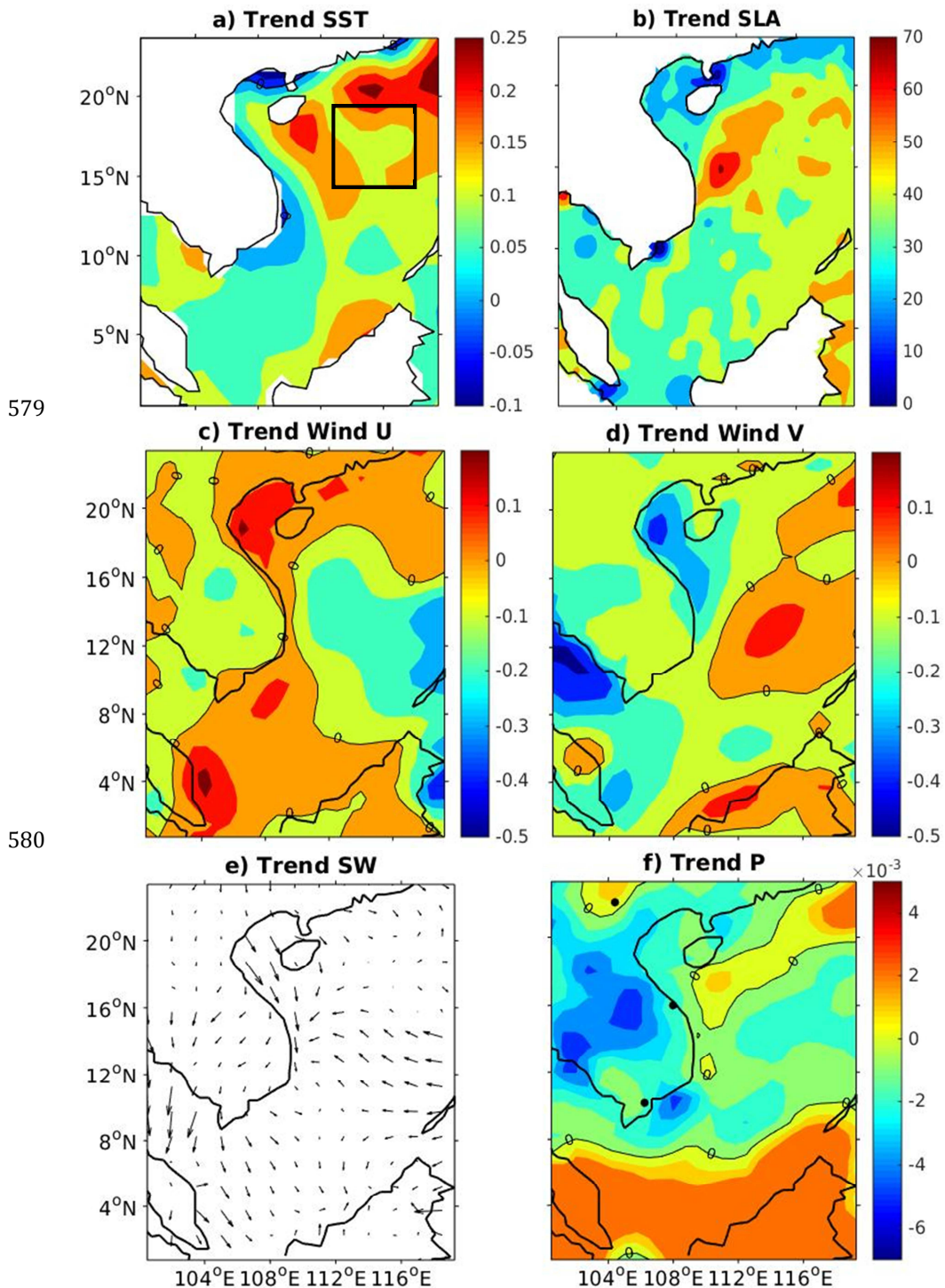
550 Trends are calculated over the total length of each dataset. Since the series differ in
551 lengths, they are also calculated over a common 27-year period (1979-2006) for most of the
552 datasets (P in situ, P and SW products from ERA-interim, WD at ST). No significant
553 differences appeared between the trends that were calculated over the entire length of the
554 dataset and over the common period (both values are discussed when possible).

555 SST. The 1982-2015 trend shows an increasing SST trend with the highest values in
556 the northeastern part of the basin and maximum values west of the Luzon Strait and along
557 the Borneo coastlines of approximately $0.24^{\circ}\text{C}/\text{decade}$ (or a total rise of 0.82°C of for the
558 period 1982-2015). A small SST decrease is observed along a very narrow coastal band off
559 central Vietnam and in the northern part of the Gulf of Tonkin of about -0.06°C per decade
560 (Fig. 13a). The computation of the wind stress curl trend (not shown here), an alias for
561 Ekman pumping trend, proves to be inconsistent with the spatial variations and even with
562 the sign of the SST trends. Fang et al. (2006) also found higher warming rates in the northern
563 deep basin and lower rates in the southern SCS with an area-mean SCS SST trend of
564 approximately $0.26^{\circ}\text{C}/\text{decade}$ (from 1982 to 2004). They further identified a period of faster
565 warming rates between 1993 and 2003 with a rate up to $0.50\pm 0.26^{\circ}\text{C}/\text{decade}$. Based on the
566 observed and simulated SCS SST from 1977 to 2013, Mei and Xie (2016) found similar rising
567 rates of SST of approximately 0.18 to $0.25^{\circ}\text{C}/\text{decade}$. For the 1960-1990 period, Casey and
568 Cornillon (2001) calculated a global ocean mean rate of $0.14\pm 0.04^{\circ}\text{C}/\text{decade}$. Assuming that
569 the recent (although different) three-decade trends can be compared, our results indicate
570 that the 1982-2015 SCS warming rate is approximately 1.7 times greater than the 1960-
571 1990 global mean rate of Casey and Cornillon (2001), and approximately 2.2 times greater
572 than the 1971-2010 global mean rate discussed by the IPCC (2014).

573 As a cautionary note, it is important to keep in mind that large discrepancies exist
574 between the published estimates of 21st century SST trends, especially in the tropical Indo-
575 Pacific. These discrepancies seem to partly result from varying estimations of ENSO



576 influence in the computation of long-term trends, as discussed in Solomon and Newman
577 (2012). The influence of ENSO on the trend computation is illustrated in the last paragraph
578 of this section.





584 The arrows denote the wind vectors, and the longest arrows are equal to $1 \times 10^{-3} \text{m/s/decade}$.
585 The color codes differ between the figures. The trends in the black square of Figure 13a are
586 discussed in the main text.

587 SLA. The map of the sea level trends for 1993-2015 shows an increasing trend
588 throughout the SCS basin with high spatial variability from 3 to 70 mm/decade and a mean
589 rising rate of approximately 41 mm/decade (Fig. 13b). A tongue of rapidly increasing rates is
590 observed from 14 to 20°N and along the longitudes 110 to 116°E, corresponding to the
591 location of the minimum of MDT (observed in Fig. 2c). This finding suggests that the sea level
592 must be rising in the low center of the cyclonic loop current that is generated by the
593 intrusion of a branch of the Kuroshio Current through the Luzon Strait (Farris and Wimbush,
594 1996; Ho et al., 2000), which results in a slowdown of the related Luzon Strait and East
595 Vietnam cyclonic eddies. Peng et al. (2013) found similar sea level rise rates of
596 approximately 39 mm/decade for the period 1993-2009 using the same data product. These
597 results are, as well as the results found here, faster than the global mean rate of sea level rise
598 of 28 ± 0.4 mm/decade (obtained for the period 1993-2003 with the TOPEX/Poseidon
599 altimeter) (Cazenave and Nerem, 2004) and the global mean sea level for 1993-2015 of
600 approximately 3.3 mm/decade that was recently obtained by Dieng et al. (2017). In line with
601 the analysis of Meyssignac et al. (2012), Cheng et al. (2016) indicated that the PDO
602 contributed to 72% of the total sea-level rise in the SCS during the 1993-2012 period. The
603 authors suggested that the intensification of the easterly winds associated with the PDO in
604 the last two decades leads to the increase in the steric sea level by deepening the
605 thermocline in the Western Tropical Pacific. Finally, they indicated that the remaining 28%
606 of the sea level trend corresponded to the global sea-level rising rate (of 18 ± 0.3
607 mm/decade).

608 SW. The trends of the two wind components (Fig. 13cd) range from -0.48 to +0.18
609 m/s/decade, respectively, with an increase of the zonal component (U) for the period 1970-



610 2015 in the northern and southern parts of the region and along the Vietnamese coastline
611 (reduced westward winds). Over the common period of measurements from 1979 to 2006,
612 the SW trends range from -4.3 to $1.7 \cdot 10^{-2}$ m/s/yr. The meridional component seems to
613 mainly weaken over the region, except in the eastern part of the SCS and above Borneo.
614 These results are consistent with the results from Fang (2006), who found an area-mean
615 trend of the zonal component of 0.56 ± 35 m/s/decade for the period 1993-2003. However,
616 we did not find an obvious trend for the meridional component. Part (not estimated here) of
617 the observed trend in the zonal wind is directly linked to the phase of the PDO, as suggested
618 by England et al. (2014) and others, since trade winds have considerably strengthened over
619 the past two decades. Figure 13e summarizes Figures 13cd in a vector form and shows that
620 the maximum rate of the trend is 1×10^{-2} m/s/decade, which occurs toward the south along
621 the Vietnamese coastlines and in the Gulf of Thailand.

622 P. The map of the linear trend of P clearly shows a rainfall deficit north of 8°N of
623 approximately 6 mm/d/decade over the period considered (1979-2015), with maximum
624 values inland (Fig. 13e). Over the common period of measurements from 1979 to 2006, the
625 decreasing trend is approximately -6.8 mm/d/decade. The Lục Yên station also shows a
626 decreasing rainfall trend (-2.64×10^{-1} mm/d/decade). However, the Đà Nẵng and Mỹ Tho
627 stations both show increasing precipitation trends with rates of 1.48×10^{-1} and 6.73×10^{-1}
628 mm/d/decade, respectively. So far, we are not able to determine the origin of the observed
629 discrepancies between the satellite and in situ measurements (as well as the discrepancies
630 about the mean, as mentioned in section 2). Comparison with other satellite products is
631 recommended here. For the period 1961 to 1998, Manton et al. (2001) also showed that the
632 number of rain days over land (at least 2 mm of rain) has significantly decreased throughout
633 Southeast Asia. They associated this decrease with the predominance of El Niño events since
634 the mid-1970s (Trenberth and Hoar, 1997).

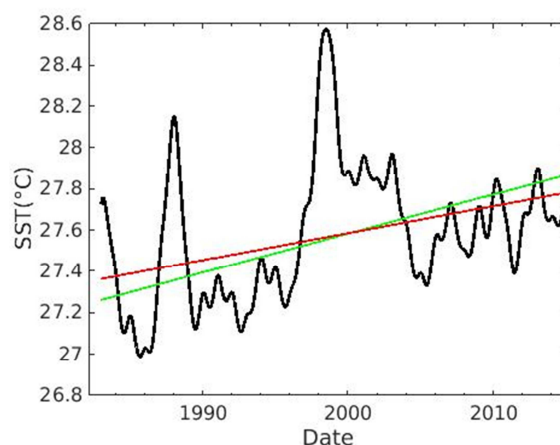


635 WD. All of the stations show small decreasing trends in water discharge. At the ST
636 Red River station, the water flux declined by $-520 \text{ m}^2/\text{s}/\text{decade}$ (representing 1.5% of the
637 mean water discharge) over the period of 1960-2010. For the common period of
638 measurement (1979 to 2006), the water flux declined by approximately $-420 \text{ m}^2/\text{s}/\text{decade}$.
639 This decreasing trend has also been emphasized by Vinh et al. (2014); it is partially due to
640 the impoundment of the Hoa Binh Dam in the late 1980s, which has decreased the water
641 flow since then. The trends at the CCV Mekong station also showed decreasing rates of -1220
642 $\text{m}^3/\text{s}/\text{decade}$ (0.98% of the mean WD) and $-1340 \text{ m}^3/\text{s}/\text{decade}$ (0.87% of the mean WD) for
643 satellite and in situ data, respectively. Lu and Siew (2006) investigated the disruption in
644 water discharge at stations on the Lower Mekong River that was induced by the cascade
645 dams in the upper part of the main stream of the Mekong River and found a declining trend
646 during the dry season. Furthermore, Xue et al. (2011) showed that the runoff of the lower
647 Mekong River was more closely connected to precipitation and ENSO in the post-dam period
648 (1993-2005) than in the pre-dam period (1950-1993). Distinguishing and isolating an effect
649 from another one (precipitation, water use and water regulation of a dam, ENSO) on water
650 discharge would provide crucial information on the behavior and possible forecasting of a
651 trend.

652 ENSO and long-term trend. The study periods and time series lengths are responsible
653 for not only the slight trend discrepancies observed between the literature and our results
654 found for each ECV but also the way the timing and the amplitude of ENSO may affect the
655 computation of long-term trends. To illustrate this issue, the 25-month Hanning filtered SST
656 and the corresponding linear trends were computed over the box $14.5\text{-}19.5^\circ\text{N}$, 112.5-
657 117.5°E roughly centered in the middle of the northern SCS (see the black square in Fig.
658 13a). Looking at Figure 14, the large SST anomalies that are characteristic of ENSO events
659 (see the ENSO indices in Fig. 10ab) clearly impact the computation of the linear trends. To
660 crudely estimate the expected effects, the 1987-1988 and 1997-1998 El Niño periods were



661 then removed, and the linear trends were recomputed. Ignoring these four El Niño years
662 increased the SST trends by as much as $1.4^{\circ}\text{C}/\text{decade}$ (from $1.06 \cdot 10^{-1} \text{ }^{\circ}\text{C}/\text{decade}$ to $1.53 \cdot 10^{-1}$
663 $^{\circ}\text{C}/\text{decade}$).



664
665 **Figure 14.** Time series of the 25-month Hanning filtered SST averaged over the box 14.5-
666 19.5°N, 112.5-117.5°E (in black), the corresponding linear trend (in red) and the linear trend
667 corresponding to the series shortened by four El Niño years (1987-88 and 1997-98) (in
668 green). The location of the box is denoted by the black square in Figure 13a.

669

670 7. Conclusion and discussion

671 In this study, we successively analyze the long-term means, standard deviations,
672 seasonal and interannual (mostly ENSO-related) variability and long-term trends of five key
673 ECVs (sea surface temperature, sea level anomaly, surface wind, precipitation, and water
674 discharge) to further document, validate, corroborate and/or complete the current scientific
675 knowledge on the climate variability in the South China Sea.

676 The analysis of the first (or first two) EOF mode(s) on each ECV clearly exhibits the
677 seasonal variability of the SCS under the influence of monsoon. In the summer, the SST is
678 found to increase throughout the basin, the SLA increases in the central and eastern parts of
679 the basin, positive rainfall anomalies are observed north of 8°N , the eastward and northward



680 wind components are stronger (reflecting the seasonal monsoon reversal) and the water
 681 discharge increases.

682 A summary of the ENSO-related changes and long-term trends of the five ECVs
 683 analyzed is provided in Table 3.

	SST 1982-2015	SLA 1993/2015	Taux 1979-2015	Tauy 1979-2015	P 1979-2015	WD ST: 1960- 2010 CCV satellites: 1996-2015 CCV in situ: 1960-2002
El Niño events	Increase basin-wide during EP	Decrease mostly in the East	Increase north of 14°N, decrease to the South	Increase north of 6°N, decrease to the South	Decrease in the South-East region	CCV: Decrease of water discharge
Trends per decade	+0.24°C	+41 mm	-0.48 to +0.18 m/s	-0.5 to +0.1 m/s	-6.8 mm/d	ST: -520 m ² /s CCV satellites: - 1220 m ³ /s CCV in situ: - 1340 m ³ /s

684 Table 3: Summary of the main modifications of five ECVs analyzed, as observed in the SCS
 685 during El Niño events and on basin-averaged long-term trends during the reported years.

686 Interestingly, it has been found that each ECV responds to specific ENSO types in
 687 different ways. The first EOF mode on SST (75% of the variance) revealed that Eastern
 688 Pacific El Niño types trigger a basin-wide warming of the SST with a 6-month lag. The second
 689 EOF mode on SST indicated a clear correlation with all types of ENSO events (represented by
 690 the SST Niño4 index). The first EOF mode on SLA (48% of the variance) showed that the SLA
 691 falls throughout the basin during an El Niño event, with a 3-month lag, and more intensely in
 692 the eastern part of SCS. Unexpectedly, the SST and SLA thus have an inverse response to
 693 ENSO. This was examined by Rong et al. (2007). Using the subsurface temperature analysis
 694 from Ishii et al. (2006), they show the coexistence of positive temperature anomalies in the
 695 upper 75 m (hence >0 SST anomalies) and negative temperature anomalies below 75 m (at
 696 least down to 700 m) during El Niño events. These out-of-phase temperature anomalies (0-



697 75 m versus 75-700 m) result in negative anomalies of the thermosteric sea level
698 component, which account for most of the negative SLA during El Niño events.

699 Previous studies have identified different potential hypotheses to explain the
700 anomalous ENSO-related SST changes. Wang et al. (2000) attributed the SCS warming to an
701 anomalous lower-tropospheric anti-cyclonic circulation located in the western North Pacific
702 through an 'atmospheric bridge'. The anomalies can persist until the following summer. Qu
703 et al. (2004) examined the heat transport through the Luzon Strait from the Pacific into the
704 SCS and suggested that this 'oceanic bridge' between the two basins was a key process in
705 conveying the impact of the Pacific ENSO into the SCS (both for SST and SLA). The respective
706 parts of the atmospheric and oceanic bridges clearly remain to be clarified.

707 The first EOF mode (64% of the total variance) of the zonal wind component revealed
708 that the wind increased eastwards north of 14°N (decreased south of 14°N) during an El
709 Niño event, with a 5-month lag. The first EOF mode (49% of the variance) of the meridional
710 wind component showed a strengthening of the northward winds north of 6°N (weakening
711 south of 6°N) during an El Niño event, with a 3-month lag. When superimposed on the strong
712 mean seasonal cycle, the El Niño events hence produce a slowdown of the winter NE and
713 summer SW monsoon winds. For precipitation, the first EOF mode (48% of the variance)
714 showed a decrease in rainfall over the entire region during El Niño phases. The linkage of
715 near-coastal in situ P stations and ENSO appeared to be stronger at lower latitudes in
716 Vietnam, for instance with P decreasing by up to 70% relative to the mean at the Da Nang
717 station during El Niño phases. Finally, water discharges taken from the Red River (at least at
718 the ST station) before the impoundment of the Hoa Binh Dam showed correlation to ENSO
719 but the post-dam impoundment period did not show a clear correlation to ENSO. The water
720 discharge from the Mekong River (at least at the CCV station) seems to respond to ENSO via
721 reduced water flow (34% of the mean for the 1997-98 El Niño event) with a 7 to 8-month
722 lag.



723 The patterns of the trends presented in the previous section provide useful elements
724 to determine the long-term variability of the ECVs. SST has risen by 0.24°C/decade basin-
725 wide (except along the coastlines of China and central Vietnam). The SLA increased with a
726 mean rising rate of 4.1 mm/yr with the highest rates in the central and the eastern parts of
727 the SCS basin, which is approximately 3 times faster than the global rate of sea level rise.
728 This corroborates the need to include data from the SCS (and semi-enclosed basins in
729 general) to improve the computation of global mean sea level trends (Dieng et al., 2015). The
730 zonal wind decreased over the period 1970-2015 by up to 0.48 m/s/decade in the eastern
731 and western parts of the region. The meridional wind strengthened southwards over the
732 entire region, except in the eastern part of the basin where the northward winds increased
733 by up to 0.18 m/s/decade. The satellite-derived precipitation decreased over the period
734 (1979-2015) by approximately 0.7 mm/d/yr over almost the entire region. In situ near-
735 coastal P stations in Vietnam showed increasing trends at lower latitudes, while the
736 northern stations showed slightly increasing to decreasing trends. All of the water
737 discharges that were observed showed small relative decreasing trends with higher rates
738 (compare to the mean) at the Red River ST station (1.5% of the mean), which is located a few
739 kilometers upstream of the city of Hanoi.

740 As a cautionary note, as discussed in England et al. (2014) and others, it is crucial to
741 consider the likely role of the PDO in the calculations of long-term trends. An inversion of the
742 sign of the PDO (e.g., in 2000) can induce a strengthening of the Pacific trade winds, leading
743 to the slowdown of the Pacific Ocean surface warming that has been observable since 2001
744 and is related to the changes in the regionally analyzed ECVs. Furthermore, as discussed in
745 the previous section and as addressed by Solomon and Newman (2012), it is essential to
746 consider the modulation of long-term trends that is induced by ENSO events (even when
747 estimated over 30 years), especially in the Indo-Pacific region.



748 Our results are based on a unique and unprecedented long-term data set we thought
749 to be relevant to each ECV. To confirm these results, it would however be fair to analyze
750 complementary data sets such as NCEP (Kalnay et al., 1996) and JRA-55 (Kobayashi et al.,
751 2015) for P, and TropFlux (Kumar et al., 2013) for P, SST and surface wind. Furthermore, the
752 growing literature that is available on the subject, and particularly the literature mentioned
753 throughout the text, has enabled us to identify mechanisms that likely account for the
754 observed variability at different time scales. Strictly quantifying the (common or not)
755 mechanisms responsible for the observed anomalies (including the ones of the 2015-16 El
756 Niño not discussed here) and trends highlighted in this paper by using outputs from
757 ocean/atmosphere dynamic models validated with our observations seems crucial to better
758 understand the seasonal, interannual and long-term variability of the region. This will be the
759 subject of another study.

760

761 **Acknowledgments:**

762 We benefited from the freely available datasets for SST ([ftp://eclipse.ncdc.noaa.gov/pub/OI-](ftp://eclipse.ncdc.noaa.gov/pub/OI-daily-v2/)
763 [daily-v2/](ftp://eclipse.ncdc.noaa.gov/pub/OI-daily-v2/)), SLA ([http://www.aviso.altimetry.fr/en/data/products/sea-surface-height-](http://www.aviso.altimetry.fr/en/data/products/sea-surface-height-products/global/msla-mean-climatology)
764 [products/global/msla-mean-climatology](http://www.aviso.altimetry.fr/en/data/products/sea-surface-height-products/global/msla-mean-climatology)), P ([http://www.ecmwf.int/en/research/climate-](http://www.ecmwf.int/en/research/climate-reanalysis/era-interim)
765 [reanalysis/era-interim](http://www.ecmwf.int/en/research/climate-reanalysis/era-interim)) and WD (<http://ctoh.legos.obs-mip.fr>). We warmly thank Vietnam's
766 Hydro-Meteorological Service for providing the inland precipitation measurements and the
767 Mekong River Commission for providing water discharge data from the gauge stations in
768 Cambodia. We are also very thankful for having had the opportunity to use the Mean
769 Dynamical Topography data provided by AVISO. Fruitful discussions with Gael Alory, Sylvain
770 Biancamaria, Frédéric Frappart, and Sylvain Ouillon, from LEGOS, help us to improve our
771 analysis.

772



References

- 773
774
775 Allan R., Lindsay J., Parker D. (1996), El Niño Southern Oscillation and climate variability.
776 CSIRO Publishing, 150 Oxford St. (PO Box 1139), Collingwood, Victoria 2066, Australia.
777 Camargo S. J., Sobel A. H. (2005) Western North Pacific Tropical Cyclone Intensity and ENSO.
778 Amer. Meteor. Soc., 18: 2996-3006., doi:10.1175/JCLI3457.1.
779 Casey K. S., Cornillon P. (2001), Global and regional sea surface temperature trends. J.
780 Climate. 14:3801-3818., doi: [http://dx.doi.org/10.1175/1520-](http://dx.doi.org/10.1175/1520-0442(2001)014<3801:GARSST>2.0.CO;2)
781 [0442\(2001\)014<3801:GARSST>2.0.CO;2](http://dx.doi.org/10.1175/1520-0442(2001)014<3801:GARSST>2.0.CO;2).
782 Cazenave A., Nerem R. S. (2004), Present-day sea level change: Observations and causes. Rev
783 Geophys., 42: RG3001, doi: 10.1029/2003RG00139.
784 Cheng X., Xie S.-P., Du Y., Wang J., Chen X., Wang J. (2016), Interannual-to-decadal variability
785 and trends of sea level in the South China Sea. Clim. Dyn., 46:3113-3126, doi:
786 10.1007/s00382-015-2756-1.
787 Chiodi A. M., Harrison A. E. (2010) Characterizing warm-ENSO variability in the equatorial
788 Pacific: An OLR-perspective. J. Climate., 23: 2428-2439, doi:
789 10.1175/2009JCLI3030.1.
790 Chiodi A. M., Harrison A. E. (2013) El Niño impacts on seasonal U.S. atmospheric circulation,
791 temperature, and precipitation anomalies: The ORL-event perspective. J. Climate., 26:
792 822-837., doi: 10.1175/JCLI-D-12-00097.1.
793 Chu C., Lu S., Chen Y. (1997), Temporal and spatial variabilities of the South China Sea
794 surface temperature anomaly. J. Geophys. Res., 102 (C9): 20937-20955, doi:
795 10.1029/97JC00982.
796 Dee D. P. et al., (2011) The ERA-Interim reanalysis: Configuration and performance of the
797 data assimilation system. Q. J. Roy. Meteor. Soc., 137(656), 553-597,
798 doi:10.1002/qj.828.
799 Deser C., Phillips A. S., Alexander M. A. (2010), Twentieth century tropical sea surface
800 temperature trends revisited. Geophys. Res. Lett., 37 (10): L10701, doi:
801 10.1029/2010GL043321.
802 Dieng, H. B., Cazenave, A., von Schuckmann, K., Ablain, M., and Meyssignac, B. (2015), Sea
803 level budget over 2005–2013: missing contributions and data errors. Ocean Sci. 11,
804 789–802.
805 Dieng, H. B., Cazenave, A., Meyssignac, B., and M. Albain (2017) New estimate of sea level rise
806 from a sea level budget approach. Geophys. Res. Lett., 44, 3744-3751,
807 doi:10.1002/2017GL073308..



- 808 England, M., S. McGregor, P. Spence, G. A. Meehl, A. Timmermann, W. Cai, A. S. Gupta, M. J.
809 McPhaden, A. Purich, and A. Santoso (2014), Recent intensification of wind-driven
810 circulation in the Pacific and the ongoing warming hiatus, *Nat. Clim. Change*, 4, 222–
811 227, doi:10.1038/nclimate210.
- 812 Fang G, Chen H, Wei Z, Wang Y, Wang X, Li C (2006) Trends and interannual variability of the
813 South China Sea surface winds, surface height, and surface temperature in the recent
814 decade. *J. Geoph. Res.* 111: CS11S16, doi: 10.1029/2005JC003276.
- 815 Farris A., Wimbush M. (1996) Wind-induced Kuroshio intrusion into the South China Sea. *J.*
816 *Oceanogr.*, 52, 771-784, doi: 10.1007/BF02239465.
- 817 Frappart F., Papa F., Marieu V., Malbêteau Y., Jordy F., Calmant S., Durand F., Bala S. (2015)
818 Preliminary assessment of SARAL/AltiKa observations over the Granges-
819 Brahmaputra and Irrawaddy Rivers. *Mar. Geod.* 38(S1): 568-580, doi:
820 10.1080/01490419.2014.990591
- 821 Frappart F., Legrésy B., Niño F., Blare F., Fuller N., Fleury S., Birol F., Calmant S. (2016) An
822 ERS-2 altimetry reprocessing compatible with ENVISAT for long-term land and ice
823 sheets studies. *Remote Sens. Environ.* 184: 558-581, doi: 10.1016/j.rse.2016.07.037.
- 824 GCOS (2016). The Global Climate Observing System: implementation needs, GCOS-200,
825 GOOS-214. World Meteorological Organization, 325 pages (Available at:
826 http://unfccc.int/files/science/workstreams/systematic_observation/application/pdf/gcos_ip_10oct2016.pdf)
827
- 828 Gobin A., Nguyen H. T., Pham V. Q., Pham H. T. T. (2016) Heavy rainfall patterns in Vietnam
829 and their relation with ENSO cycles. *Int. J. Climatol.* 36: 1686-1699, doi:
830 10.1002/joc.4451.
- 831 Hanley D. E., Bourassa M. A., O'Brien J. J., Smith S. R., Spade E. R. (2003) A quantitative
832 evaluation of ENSO indices. *J. Climate*, 16: 1249-1258, doi:
833 [http://dx.doi.org/10.1175/1520-0442\(2003\)16<1249:AQEOIEI>2.0.CO](http://dx.doi.org/10.1175/1520-0442(2003)16<1249:AQEOIEI>2.0.CO)
- 834 Hannachi A., Jolliffe I. T., Stephenson D. B. (2007) Empirical orthogonal functions and related
835 techniques in atmospheric sciences: A review. *Int. J. Climatol.*, 27, 1119-1152, doi:
836 10.1002/joc.1499.
- 837 Ho C.-R., Zheng Q., Soong Y. S., Kuo N.-J., Hu J.-H. (2000) Seasonal variability of sea surface
838 height in the South China Sea observed with TOPEX/Poseidon altimeter data. *J.*
839 *Geophys. Res.* 105: 13981-13990, doi: 10.1029/2000JC900001.
- 840 Huynh H.-N., Alvera-Azcarate A., Barth A., Beckers J.-M. (2016), Reconstruction and analysis
841 of long-term satellite-derived sea surface temperature for the South China Sea. *J.*
842 *Oceanogr.*, 1-20, doi: 10.1007/s10872-016-0365-1.



- 843 IPCC Fourth Assessment Report (AR4): Contribution of Working Group I, II and III to the
844 Fourth Assessment Report of the Intergovernmental Panel on Climate Change. Core
845 Writing Team, Pachauri R. K. And , Reisinger A. (Eds), IPCC, Geneva, Switzerland. Pp
846 104.
- 847 Ishii, M., Kimoto, M., Sakamoto, S., Iwasaki, S.-I. (2006) Steric sea level changes estimated
848 from historical ocean subsurface temperature and salinity analyses. *J. Oceanogr.*, 62
849 (2), 155-170.
- 850 Juneng L., Tangang F. T. (2005), Evolution of ENSO-related rainfall anomalies in Southeast
851 Asia region and its relationship with atmosphere-ocean variations in Indo-Pacific
852 sector. *Clim. Dynam.*, 25: 337-350, doi: 10.1007/s00382-005-0031-6.
- 853 Kalnay E, et al. (1996) The NCEP/NCAR 40-year reanalysis project. *Bulletin of American*
854 *Meteorology Society*, 77(3), 437-471, doi: [https://doi.org/10.1175/1520-](https://doi.org/10.1175/1520-0477(1996)077<0437:TNYRP>2.0.CO;2)
855 [0477\(1996\)077<0437:TNYRP>2.0.CO;2](https://doi.org/10.1175/1520-0477(1996)077<0437:TNYRP>2.0.CO;2).
- 856 Klein S. A., Soden B. J., Lau N.-C. (1999), Remote sea surface temperature variations during
857 ENSO: Evidence for a tropical atmospheric bridge. *J. Climate*, 12, 917-932, doi:
858 [http://dx.doi.org/10.1175/1520-0442\(1999\)012<0917:RSSTVD>2.0.CO;2](http://dx.doi.org/10.1175/1520-0442(1999)012<0917:RSSTVD>2.0.CO;2).
- 859 Kobayashi S, et al. (2015) The JRA-55 Reanalysis: General specifications and basic
860 characteristics. *Journal of the Meteorological Society of Japan*, 93, 5-48, doi:
861 <http://doi.org/10.2151/jmsj.2015-001>.
- 862 Kouraev A. V., Zakharova E. A., Samain O., Mognard N. M., Cazenave A. (2004), Ob's river
863 discharge from TOPEX/Poseidon satellite altimetry (1992-2002). *Remote Sens.*
864 *Environ.*, 93, 238-245, doi: <http://doi.dx.org/10.1016/j.rse.2004.07.007>.
- 865 Kumar Praveen B., Vialard J., Lengaigne M., Murty V. S. N., McPhaden M.J. (2012) TropFlux:
866 air-sea fluxes for the global tropical oceans – description and evaluation. *Clim. Dyn.* 38,
867 1521, doi:10.1007/s00382-011-1115-0.
- 868 Leuliette E. W., Willis J. K. (2011), Balancing the sea level budget. *Oceanography*. 24(2):122-
869 129., doi:10.5670/oceanog.2011.32
- 870 Liu Q., Jiang X., Xie S.-P., Liu W. T. (2004) A gap in the Indo-Pacific warm pool over the South
871 china Sea in borel winter: Seasonal development and interannual variability. *J.*
872 *Geophys. Res.*, 109(C07012), doi:10.1029/2003JC002179.
- 873 Lu X.X, Siew R.Y. (2006), Water discharge and sediment flux changes over the past decades
874 in the Lower Mekong River: possible impact of the Chinese dams. *Hydrol. Earth. Syst.*
875 *Sci.*, 10: 181-195, doi: hal-00304834.
- 876 Manton M. J., Della-Marta P. M., Haylock M. R., Hennessy K. J., Nicholls N., Chambers L. E.,
877 Collins D. A., Daw G., Finet A., Gunawan D., Inape K., Isobe H., Kestin T. S., Lefale P.,



- 878 Leyu C. H., Lwin T., Maitrepierre L., Ouprasitwong N., Page C. M., Pahalad J., Plummer
879 N., Salinger M. J., Suppiah R., Tran V. L., Trewin B., Tibig I., Yee D. (2001), *Int J*
880 *Climatol.*, 21:269-284, doi: 10.1002/joc.610.
- 881 Mantua N. J., Hare S. R. (2002), The Pacific Decadal Oscillation. *J. Oceanogr.* 58(1), 35-44.
- 882 Mei W., Xie S.-P. (2016), Intensification of the landfalling typhoons over the northwest
883 Pacific since the late 1970s. *Nat. Geosci.*, 9: 753-758, doi:10.1038/NGEO2792.
- 884 Meyssignac B., Llovel W., Cazenave A., Salas-Melia D., Becker M. (2012) Tropical Pacific
885 spatial trend patterns in observed sea level: internal variability and/or anthropogenic
886 signature? *Climate of the Past.* 8:787-802. doi: 10.5194/cp-8-787-2012
- 887 Nguyen D.-Q., Renwick J., McGregor J. (2014), Variations of surface temperature and rainfall
888 in Vietnam from 1971 to 2010. *Int. J Climatol.*, 34, 249-264, doi: 10.1002/joc.3684.
- 889 North G. R., Bell T. L., Cahalan R. F., Moeng F. J. (1982), Sampling Errors in the Estimation of
890 Empirical Orthogonal Functions. *Amer. Meteor. Soc.*, 110: 699-706, doi:
891 [http://dx.doi.org/10.1175/1520-0493\(1982\)110<0699:SEITEO>1.0.CO;2](http://dx.doi.org/10.1175/1520-0493(1982)110<0699:SEITEO>1.0.CO;2).
- 892 Peng D., Palanisamy H., Cazenave A., Meyssignac B. (2013), Interannual Sea Level Variations
893 in the South China Sea over 1950-2009. *Mar. Geod.*, 36: 164-182, doi:
894 <http://dx.doi.org/10.1080/01490419.2013.771595>.
- 895 Qu T. (2001) Role of the ocean dynamics in determining the mean seasonal cycle of the
896 South China Sea surface temperature. *J Geophys. Res.*, 106: 6943-6955, doi:
897 10.1029/2000JC000479.
- 898 Qu T., Kim Y. Y., Yaremchuk M., Tozuka T., Ishida A., Yamagata T. (2004) Can Luzon Strait
899 Transport play a role in conveying the impact of ENSO to the South China Sea? *J.*
900 *Climate*, 17: 3644-3657, doi: [https://doi.org/10.1175/1520-](https://doi.org/10.1175/1520-0442(2004)017<3644:CLSTPA>2.0.CO;2)
901 [0442\(2004\)017<3644:CLSTPA>2.0.CO;2](https://doi.org/10.1175/1520-0442(2004)017<3644:CLSTPA>2.0.CO;2).
- 902 Qu T., Song T., Yamagata T. (2009) An introduction to the South China Sea throughflow : its
903 dynamics, variability and application for climate. *Dyn. Atmosph. Oceans*, 47, 3-14.
- 904 Räsänen T. A., Kumm M. (2013), Spatiotemporal influences of ENSO on precipitation and
905 flood pulse in the Mekong River Basin. *J of Hydrol.*, 476, 154-168, doi:
906 <http://dx.doi.org/10.1016/j.hydrol.2012.10.028>.
- 907 Räsänen T. A., Lindgren V., Guillaume J. H. A., Buckley B. M., Kumm M. (2016) On the spatial
908 and temporal variability of ENSO precipitation and drought teleconnection in mainland
909 Southeast Asia. *Clim. Past.*, 12, 1889-1905, doi: 10.5194/cp-12-1889-2016..
- 910 Rayner N. A., Parker D. E., Horton E. B., Folland C. K., Alexander L. V., Rowell D. P., Kent E. C.,
911 Kaplan A. (2003), Global analysis of sea surface temperature, sea ice, and night



- 912 marine air temperature since the late nineteenth century. *J. Geophys. Res.*, 108(D14):
913 4407, doi: 10.1029/2002JD002670.
- 914 Reynolds R. W., Smith T. M., Liu C., Chelton D. B., Casey K. S., Schlax M. G. (2007) Daily High-
915 Resolution-Blended Analyses for Sea Surface Temperature. *American Meteorological*
916 *Society*. 20: 5473, 5496, doi: <http://dx.doi.org/10.1175/2007/JCLI1824.1>.
- 917 Rio M.-H., Mulet S., Picot N. (2014), Beyond GOCE for the ocean circulation estimate:
918 Synergetic use of altimetry, gravimetry, and in situ data provides new insight into
919 geostrophic and Ekman currents. *Geophys. Res. Lett.*, 41: 8918-8925, doi:
920 10.1002/2014GL061773.
- 921 Rong Z., Liu Y., Zong H., Cheng Y. (2007), Interannual sea level variability in the South China
922 Sea and its response to ENSO. *Global Planet. Change*, 55, 257-272, doi:
923 <http://dx.doi.org/10.1016/j.gloplacha.2006.08.001>.
- 924 Saji N. H., Goswami B. N., Vinayachandran P. N., Yamagata T. (1999), A dipole mode in the
925 tropical Indian Ocean. *Nature*, 401: 360-363.
- 926 Sing A., Delcroix T., Cravatte A. (2011) Contrasting the flavors of El Niño Southern Oscillation
927 using sea surface salinity observations. *J. Geophys. Res.*, 116: C06016,
928 doi:10.1029/2010JC006862.
- 929 Solomon A., Newman M. (2012), Reconciling disparate twentieth-century Indo-Pacific ocean
930 temperature trends in the instrumental record. *Nat. Clim. Change.*, 2: 691-697, doi:
931 10.1038/nclimate1591.
- 932 Tan W., Wang X., Wang W., Wang C., Zuo J. (2016) Different Responses of Sea Surface
933 Temperature in the South China Sea to Various El Niño Events during Boreal Autumn.
934 *J. Climate.*, 29, 1127-1142, doi: <http://dx.doi.org/10.1175/JCLI-D-15-0338.1>.
- 935 Trenberth K. E., Hoar T. J. (1997) El Niño and climate change. *Geophys. Res. Lett.* 24: 3057-
936 3060, doi: 10.1020/97GL03092.
- 937 Trenberth K. E., Stepaniak D. P. (2001) Indices of El Niño Evolution. *J. Climate.*, 14 : 1697-
938 1701., doi: [http://dx.doi.org/10.1175/1520-](http://dx.doi.org/10.1175/1520-0442(2001)014<1697:LIOENO>2.0.CO;2)
939 [0442\(2001\)014<1697:LIOENO>2.0.CO;2](http://dx.doi.org/10.1175/1520-0442(2001)014<1697:LIOENO>2.0.CO;2).
- 940 Tuen K. L. (1994) Monitoring of sea surface temperature in the South China Sea.
941 *Hydrobiologia*. 285: 1-5, doi: 10.1007/978-94-011-0958-1_1.
- 942 Vinh V. D., Ouillon S., Thanh T. D., Chu L. V. (2014), Impact of the Hoa Binh dam (Vietnam) on
943 water and sediment budgets in the Red River basin and delta. *Hydrolog. Earth Sci.*, 18:
944 3987-4005, doi: 10.5194/hess-18-3987-2014.



- 945 Wang B., LinHo (2002), Rainy season of the Asian-Pacific summer monsoon. *J. Climate.*, 15,
946 386-398, doi:
947 [http://dx.doi.org/10.1175/15200442\(2002\)015<0383:RSOTAP>2.0.CO;2](http://dx.doi.org/10.1175/15200442(2002)015<0383:RSOTAP>2.0.CO;2).
- 948 Wang B., H, uang F., Wu Z., Yang J., Fu X., Kikuchi K. (2009) Multi-scale climate variability of
949 the South China Sea monsoon: A review. *Dyn. Atmosph. Oceans*, 47, 3-14
- 950 Wang B., Wu R., Fu X. (2000) Pacific-East Asian Teleconnection: How does ENSO affect East
951 Asian climate? *J. Climate*, 13: 1517-1536, doi: [https://doi.org/10.1175/1520-](https://doi.org/10.1175/1520-0442(2000)013<1517:PEATHD>2.0.CO;2)
952 [0442\(2000\)013<1517:PEATHD>2.0.CO;2](https://doi.org/10.1175/1520-0442(2000)013<1517:PEATHD>2.0.CO;2)
- 953 Wang C., Wang W., Wang D., Wang Q. (2006), Interannual variability of the South China Sea
954 associated with El Niño. *J. Geophys. Res.*, 111: C03023, doi: 10.1029/2005JC003333.
- 955 Wang C., Xie S.-P., Carton J. A. (2004) A global survey of ocean-atmosphere interaction and
956 climate variability, in *Earth Climate: The Ocean-Atmosphere Interaction* edited by
957 Wang C et al., 1-19, AGU, Washington D C.
- 958 Wyrтки, K., 1961: Physical oceanography of the Southeast Asian waters. *Naga Rep.* 2, 195 pp.
959 [Available from: <https://escholarship.org/uc/item/49n9x3t4>].
- 960 Wu C.-H., June Chang C.-W. (2005) Interannual variability of the South China Sea in a data
961 assimilation model. *J. Geophys. Res.*, 32:LI7611, doi:10.1029/2005GL023798
- 962 Wu L., Wang B., Geng S. (2005) Growing typhoon influence on east Asia. *Geophys. Res. Lett.*,
963 32 (18), LI8703, doi:10.1029/2005GL022937.
- 964 Yang Y., Xie S.-P., Du Y., Tokinaga H. (2015) Interdecadal difference of interannual variability
965 characteristics of South China Sea SSTs associated with ENSO. *Amer Meteor Soc.* 28:
966 7145-7160, doi:10.1175/JCLI-D-15-0057.1
- 967 Xue Z., Liu J. P., Ge Q. (2011) Changes in hydrology and sediment delivery of the Mekong
968 River in the last 50 years: connection to damming, monsoon, and ENSO. *Earth Surf.*
969 *Proc. Land.*, 36: 296-308, doi: 10.1002/esp.2036.
- 970 Zhuang W., Xie S.-P., Wang D., Taguchi B., Aiki H., Sasaki H. (2010) Intraseasonal variability in
971 sea surface height over the South China Sea. *J. Geophys. Res.*, 115: C04010,
972 doi:10.1029/2009JC005647.
- 973